NUMERICAL SIMULATION OF ION TRANSPORT MEMBRANE REACTORS: OXYGEN PERMEATION AND TRANSPORT AND FUEL CONVERSION

Jongsup Hong, Patrick Kirchen, Ahmed F. Ghoniem *

Department of Mechanical Engineering, Massachusetts Institute of Technology,

77 Massachusetts Avenue, Cambridge, MA 02139, USA

Key Words: Ion transport membrane reactor; High temperature membrane reactor; Oxygen permeation; Numerical analysis; Modeling; Surface exchange; Bulk diffusion.

ABSTRACT

Ion transport membrane (ITM) based reactors have been suggested as a novel technology for several applications including fuel reforming and oxy-fuel combustion, which integrates air separation and fuel conversion while reducing complexity and the associated energy penalty. To utilize this technology more effectively, it is necessary to develop a better understanding of the fundamental processes of oxygen transport and fuel conversion in the immediate vicinity of the membrane. In this paper, a numerical model that spatially resolves the gas flow, transport and reactions is presented. The model incorporates detailed gas phase chemistry and transport. The model is used to express the oxygen permeation flux in terms of the oxygen concentrations at the membrane surface given data on the bulk concentration, which is necessary for cases when mass transfer limitations on the permeate side are important and for reactive flow modeling. The simulation results show the dependence of oxygen transport and fuel conversion on the geometry and flow parameters including the membrane temperature, feed and sweep gas flow, oxygen concentration in the feed and fuel concentration in the sweep gas.

* Corresponding author. Tel.: +1 617 253 2295; Fax: +1 617 253 5981
Email address: ghoniem@mit.edu (Ahmed F. Ghoniem)

1. INTRODUCTION

Ion transport membranes (ITM), whose material is characterized by high ionic and electronic conductivity, have been demonstrated for air separation and oxygen production, and to a lesser extent for fuel reforming and oxidation [1, 2]. Since the 1980s when mixed-conducting ceramic membranes were introduced [3-6], extensive research has been performed to improve oxygen permeation rates [7-13]. In the course of these experimental activities, a reactive gas such as methane has been employed on the permeate side to increase the chemical potential gradient by consuming the permeated oxygen and to maintain the membrane temperature, and thus to enhance oxygen permeation rates. Recent research shows that the oxygen permeation rate in which air separation and oxidation reactions take place simultaneously increases by a factor of 2 to 9 [14-18] compared to that of the separation-only case.

Incorporating ITMs in different reactors has been suggested for different applications because of the high purity of oxygen produced in the separation process as oxygen is selectively added to the permeate side through ion transport. In a reactive process, the high purity oxygen leads to better control over the quality of the product. ITM reactors not only improve oxygen permeation rates, but also deliver product streams with higher selectivity than conventional reactors [19]. The complete conversion of fuel with pure oxygen yields only carbon dioxide and water [20, 21]. By condensing water, the exhaust stream contains high purity carbon dioxide. Therefore, oxy-fuel combustion, an important technology in power generation with carbon capture, can be performed in an ITM reactor without the need for extra purification for the exhaust stream. In another application, partial oxidation using the oxygen produced by the membrane can be used to reform a fuel to a synthesis gas composed of carbon monoxide and hydrogen [22-26]. As oxygen is introduced uniformly into the permeate side where partial oxidation takes place, ITM reactors achieve a higher carbon monoxide selectivity than typical reactors (e.g., co-fed, fixed bed reactors). Multiple methods have been investigated for production of hydrogen, and ITM reactors with partial oxidation of fuel is one of them. Another application of ITM reactors is to produce higher hydrocarbons such as ethane and ethylene [27, 28], which is called oxidative coupling. By enabling methane to react with oxygen ions in the crystalline structure, rather than gaseous molecular oxygen, deep oxidation of the fuel is avoided and higher order hydrocarbons can be produced.

Oxygen permeation rate and hydrocarbon conversion/product selectivity are strongly coupled through the local oxygen chemical potential in the vicinity of membrane surfaces, as well as the membrane temperature [29]. In case a

reaction takes place on the permeate side, the local oxygen concentration in the vicinity of the membrane is influenced by oxidation reactions and hence cannot be approximated by the bulk stream oxygen concentrations measured at the permeate stream outlet side. With respect to fuel conversion, since oxygen is introduced at a finite rate, its local concentration plays an important role in determining the overall reaction rate and reaction products. Moreover, the heat released along with the location of reaction zone affects the temperature profile and the membrane temperature. Therefore, it is important to perform experimental studies and to develop modeling approaches that can spatially resolve the thermochemical field in the immediate neighborhood of the membrane. So far only a limited number of studies have been conducted [21, 24, 25, 30].

Given the novelty of the technology, only few modeling studies have been published. Tan et al. [21] and Jin et al. [30] assumed a plug flow to model their reactor, and negligible temperature changes due to oxidation reactions. They showed how oxygen permeation and fuel conversion rates vary with the operating temperature, feed air and fuel flow rates and reactor geometry. Smit et al. [24] presented a rigorous model, but neglected gas phase mass transfer and spatial variations of temperature. Tan et al. [25] considered the spatially resolved oxygen concentrations and temperature in a membrane reactor for partial oxidation of methane, and solved for the product selectivity and hydrocarbon conversion as a function of the operating parameters including temperature, methane flow rate, membrane tube diameter and membrane thickness. They implemented a three-step reaction mechanism, and based their oxygen permeation model on kinetic parameters obtained using the bulk stream parameters by Xu and Thomson [31]. As we show in this paper, permeation flux models parameterized in terms of the oxygen concentration in the bulk may not be applicable in the case of a reactive flow on the permeate side. We also show that detailed chemistry is necessary to account for important phenomena such as fuel pyrolysis.

In this paper, we formulate a computational model for oxygen transport and fuel conversion in a set up frequently used to study the impact of the operating conditions on oxygen permeation across an ITM. Our computational model incorporates detailed chemical kinetics and multistep transport in the gas phase. We start with the development of an oxygen permeation flux model parameterized in terms of the local oxygen partial pressures in the vicinity of the membrane. We show that it is important to use permeation flux models based on the values of the oxygen concentration close to the membrane surface, and show how experimental measurements of the flux and the oxygen concentration at the bulk can be used to calculate the oxygen concentration at the surface. The spatially resolved flow field is used to estimate the kinetic

parameters of the membrane. Next we use the permeation flux model to study the dependence of oxygen transport on the operating conditions including the presence of a fuel in the sweep gas. An overview of the fundamentals of oxygen ion transport processes and the oxygen transport mechanism considered in this study is discussed in Section 2. In Section 3, the numerical model and the numerical scheme employed in this study are described. Section 4 summarizes the methodology to parameterize the spatially resolved oxygen permeation flux expression based on the local oxygen chemical potential at the membrane surface. In Section 5, the impact of the operating conditions including the membrane temperature, feed and sweep gas flow rates, sweep gas channel height, oxygen concentration in the feed air and chemical reactions on the oxygen transport are presented and discussed.

2. OXYGEN TRANSPORT MECHANISM

The oxygen permeation mechanism is incorporated into the coupled thermochemical-fluid dynamic model described in Section 3, using a single step expression. In this expression, the oxygen permeation flux is described in terms of the gas phase parameters, that is, the oxygen partial pressure on both sides of the membrane. This expression is derived in this section starting with a multi-step mechanism. Figure 1 shows the important steps of oxygen transport across the membrane: the gas phase mass transfer, surface exchange and bulk diffusion, following the chemical potential gradient. The gas phase mass transfer is described using a fluid dynamic model, while surface exchange and bulk diffusion are based on surface species and bulk phase ions inside the membrane [32, 33]. Instead of keeping track of the surface species and bulk phase ions, a single step expression that accounts for surface exchange on both sides of the membrane and bulk ion diffusion across the ITM is developed. Implementing a single-step oxygen transport expression across the membrane improves the computational efficiency of the overall model and enables studying important oxygen transport steps and their dependence on other gas-phase flow parameters.

2.1. Overview of Oxygen Transport Processes

Based on the difference in the oxygen chemical potentials between the feed side and the permeate side, the membrane temperature and its ambipolar conductivity, oxygen migrates from the high pressure feed side to the low pressure permeate side, according to the overall transport processes summarized as follows [34-37] (refer to Figure 1 for stream points, (a) through (f)):

i. **(a) to (b):** gaseous oxygen mass transfer (advection and diffusion) from the feed stream to the membrane surface

ii. **(b) to (c):** adsorption onto the membrane surface, dissociation and ionization of oxygen molecules and subsequent incorporation of the ions into the lattice vacancies (feed side surface exchange)

iii. **(c) to (d):** transport of lattice oxygen ions through the membrane (bulk diffusion)

iv. **(d) to (e):** association of lattice oxygen ions to oxygen molecules and desorption from the membrane surface into the gas phase (permeate side surface exchange)

v. **(e) to (f):** gaseous oxygen mass transfer (advection and diffusion) from the membrane surface to the permeate stream

The gaseous mass transfer processes (i and v) are modeled using homogeneous gas species conservation equations (continuity, momentum and energy). Global reaction kinetics is used to approximate the surface exchange (ii and iv), while the bulk diffusion (iii) is governed by internal defect reactions or oxygen vacancy transport.

2.1.1. Gas phase mass transfer

The gas phase mass transfer plays an important role in oxygen transport especially when the flow rate is low enough to result in a relatively thick boundary layer. A high flow rate of the sweep gas or feed gas reduces the corresponding boundary layer next to the membrane surface. In this case, the oxygen concentration profile in the gas is nearly uniform and its effect on the gas phase mass transfer is insignificant. This is the typical assumption in some ITM research. However, the flow rate in typical ITM reactors is small such that the required stoichiometry of the chemical reactions is satisfied, and accordingly the boundary layer thicknesses can be large depending on the length scale of the reactor. In this case, the gas phase mass transfer has a significant impact on the oxygen concentration profile, especially in the permeate side where oxidation reactions occur. Recent research has highlighted the importance of the gas phase mass transfer and the non-uniform oxygen chemical potentials next to the membrane surface [38].

In typical ITM permeation measurements, the oxygen permeation rates are characterized in terms of the feed stream inlet partial pressure or oxygen concentration and the same parameters at the sweep gas outlet. Oxygen concentrations measured at these two points may not be the same as those at the two sides of the membrane surface. By ignoring the effects of the gas phase mass transfer, it is assumed that the measurements at the points away from the vicinity

of the membrane surface are the same as the local values near the membrane ((b) and (e) in Figure 1). Thus, while the resulting expressions may be sufficient for describing similar set ups, they are not general [38] and the local oxygen concentration profiles should be determined in order to recast these expressions in terms of the local values at the vicinity of the membrane surface.

2.1.2. Surface exchange

The surface exchange processes connect the gas phase oxygen molecules in the immediate neighborhood of the membrane with the membrane surface species. As mentioned above, gaseous oxygen molecules adsorb onto the membrane surface, dissociated and ionized by reacting with available free electrons from the lattice, hence occupying an oxygen vacancy and forming two electron holes [1]. The reverse processes take place on the permeate side of the membrane after the oxygen ions transport across the membrane by bulk diffusion as discussed in Section 2.1.3. The global surface exchange reaction describing these processes is,

$$\frac{1}{2}O_2 + V_O^{\bullet\bullet} \xleftrightarrow{k_f/k_r} O_O^x + 2h^{\bullet} \tag{1}$$

The conventional Kroger-Vink notation is used here for the lattice species and defects where $V_O^{\bullet\bullet}$ is the oxygen vacancy; O_O^x is the lattice oxygen ion; $h^{\bullet}$ is the electron hole, and k_f and k_r are the reaction rates of forward and backward reactions of expression (1), respectively. Although a multistep kinetic mechanism written in terms of more elementary reactions exist [39, 40], the expression (1) is sufficient to model the overall surface exchange process on both sides of the membrane [41, 42].

The law of mass action, with reaction rates based on the activation energy and membrane temperature, is used to approximate the oxygen surface exchange kinetics [39-41, 43, 44]. Based on the transition state theory, the reaction rates are typically expressed in an Arrhenius form,

$$k_i = \xi \frac{\kappa_B T_{mem}}{h_p} \exp\left(\frac{-E_A}{RT_{mem}}\right) \tag{2}$$

where k_i represents either forward (k_f) or backward (k_r) reaction rate of the surface exchange reactions, as described in expression (1); ξ is a transmission coefficient; κ_B is the Boltzmann constant; h_P is the Planck constant; E_A is the activation energy; T_{mem} is the membrane temperature and R is the universal gas constant. Surface exchange processes are strongly dependent on the membrane temperature and the activation energy which is a function of surface properties.

Typical mixed-conducting membranes have a substantially high electronic conductivity, and hence the electron hole concentrations are constant throughout the ITM at steady state. It can be assumed that the surface exchange reactions are no longer dependent on the concentration of electron holes. As a result, the backward reaction of surface exchange, expressed in (1), becomes pseudo-zero order at steady state under isothermal operations [45]. Then, based on the global reaction (1) and the reaction rate expression (2), the oxygen permeation rate by the surface exchange reaction on each side of the membrane can be expressed as,

$$J_{O_2} = k_f P_{O_2,feed,(s)}^{0.5} C_{V_O^{\bullet\bullet},feed} - k_r \quad \text{: Feed side} \tag{3}$$

$$J_{O_2} = k_r - k_f P_{O_2,sweep,(s)}^{0.5} C_{V_O^{\bullet\bullet},sweep} \quad \text{: Permeate side} \tag{4}$$

where $P_{O_2,feed,(s)}$ and $P_{O_2,sweep,(s)}$ stand for the oxygen partial pressures evaluated at the membrane surfaces in both the feed and sweep gas sides, respectively; $C_{V_O^{\bullet\bullet},feed}$ and $C_{V_O^{\bullet\bullet},sweep}$ are the molar concentrations of oxygen vacancies on the membrane surfaces in both feed and sweep gas sides, respectively. Note that (3) and (4) are equal at steady state. Depending on how the expressions in (3) and (4) are simplified or the reaction rate (2) is approximated, different empirical correlations for the surface exchange processes have been proposed [41, 43, 44, 46].

2.1.3. Bulk diffusion

When both ionic and electronic conductivities of the membrane are sufficiently high, oxygen ion transport through the membrane does not need an external electrical circuit. The permeation of oxygen ions is charge compensated by a flux of electrons in the reverse direction. Because these membranes are dense/gas-tight, direct permeation of gaseous oxygen

molecules is prohibited, and only ionized oxygen can move across them. A number of different mechanisms have been discussed to explain bulk ion diffusion across an ITM, among which the vacancy transport mechanism is widely used [45]. Only mobile ionic defects can move from one lattice position to another, and the oxygen vacancy and electron hole are the two charged defects in ITM. When an oxygen vacancy moves to the site occupied by an oxygen ion, the oxygen ion is relocated to the site released by the oxygen vacancy. The transport of charged defects at steady state under an electrochemical potential gradient is described by the Nernst-Planck equation,

$$J_i = -\frac{\sigma_i}{(z_i F)^2} \nabla \eta_i \tag{5}$$

where σ_i is the ionic conductivity of charged defects *i*; z_i is the charge number of charged defects *i*; F is the Faraday constant; $\nabla \eta_i$ is the electrochemical potential gradient of charged defects *i*, which can be expressed as,

$$\nabla \eta_i = \nabla \mu_i + z_i F \nabla \phi \tag{6}$$

where $\nabla \mu_i$ is the chemical potential gradient of charged defects *i*, and $\nabla \phi$ is the electric potential gradient across the membrane. In general, transverse variations of charged defect concentrations are negligible in a thin mixed ionic-electronic conductor, and a one-dimensional approximation ((c) to (d) in Figure 1) can be implemented. Expression (5) and (6) are thus written as,

$$J_i = -\frac{\sigma_i}{(z_i F)^2} \left[RT \frac{\partial \ln C_i}{\partial y} + z_i F \frac{\partial \phi}{\partial y} \right] \tag{7}$$

where C_i is the molar concentration of charged defects *i*. The Nernst-Einstein relation explains σ_i, as shown below.

$$\sigma_i = \frac{(z_i F)^2 D_i C_i}{RT} \tag{8}$$

where D_i is the diffusivity of charged defects *i*. Depending on the simplification applied to the Nernst-Einstein relation for the ionic conductivity, different empirical correlations for bulk diffusion have been proposed [42, 46-49]. Due to the high electronic conductivity of mixed-conducting ceramic membranes, the concentration of electrons is maintained constant across the ITM at steady state. As a result, the oxygen permeation is limited by the transport of oxygen vacancy (i.e., ionic conductivity). In addition, the membrane is electrically neutralized, and the electric potential gradient is generally neglected at steady state. Then, assuming a linear variation of oxygen vacancy concentration across the ITM, the oxygen vacancy transport can be expressed using expression (7) and (8) as,

$$J_{V_O^{\bullet\bullet}} = -D_{V_O^{\bullet\bullet}} \frac{\partial C_{V_O^{\bullet\bullet}}}{\partial y} = -\frac{D_{V_O^{\bullet\bullet}}}{L}\left(C_{V_O^{\bullet\bullet},sweep} - C_{V_O^{\bullet\bullet},feed}\right) \tag{9}$$

where L is the membrane thickness. Note that the oxygen vacancy diffusion coefficient, $D_{V_O^{\bullet\bullet}}$, is dependent on the temperature and the crystalline structure of the membrane. At steady state, under isothermal operations and for small differences in the oxygen partial pressures, the diffusion coefficient is assumed to be constant across the membrane. Based on the stoichiometry (refer to expression (1)), the oxygen permeation rate by bulk diffusion becomes,

$$J_{O_2} = -\frac{1}{2} J_{V_O^{\bullet\bullet}} = \frac{D_{V_O^{\bullet\bullet}}}{2L}\left(C_{V_O^{\bullet\bullet},sweep} - C_{V_O^{\bullet\bullet},feed}\right) \tag{10}$$

Expression (10) shows that the oxygen permeation rate by bulk diffusion is governed by the ionic conductivity, temperature and the chemical potential gradient of oxygen vacancies across the membrane.

2.2. Reduction in Terms of the Partial Pressures

As proposed by Xu and Thomson [31], at steady state, an expression that combines surface exchange on the feed and permeate sides and bulk diffusion in terms of the oxygen partial pressures can be derived. At steady state, expression (3), (4) and (10) are equal. Combining these expressions, we obtain the desired form:

$$J_{O_2} = \frac{D_{V_O^{\bullet\bullet}} k_r \left(P_{O_2,feed,(s)}^{0.5} - P_{O_2,sweep,(s)}^{0.5} \right)}{2Lk_f \left(P_{O_2,feed,(s)} P_{O_2,sweep,(s)} \right)^{0.5} + D_{V_O^{\bullet\bullet}} \left(P_{O_2,feed,(s)}^{0.5} + P_{O_2,sweep,(s)}^{0.5} \right)} \tag{11}$$

Note that expression (11) describes the important dependence of the oxygen permeation rate on the surface exchange (i.e., the membrane temperature and the activation energy) and the bulk diffusion (i.e., the ionic conductivity, chemical potential gradient and membrane temperature) as discussed in Section 2.1.2 and Section 2.1.3 and can be used under surface exchange limited and bulk diffusion limited conditions.

To use the single step expression in the fluid dynamic model, the diffusion coefficient of oxygen vacancies, $D_{V_O^{\bullet\bullet}}$, and the surface exchange reaction rates, k_f and k_r, must be known. These can be expressed in an Arrhenius form as shown below,

$$\Theta_i = \psi_i \exp\left(\frac{-E_{A,i}}{RT_{mem}} \right) \qquad \text{where } \Theta_i = D_{V_O^{\bullet\bullet}}, k_f, k_r \tag{12}$$

The pre-exponential factor, ψ_i, and the activation energy, $E_{A,i}$, are derived from experimental data (i.e., oxygen permeation rates). Furthermore, the oxygen partial pressures used in expression (11) should be evaluated in the immediate vicinity of the membrane surface (i.e., $P_{O_2,feed,(s)}$ and $P_{O_2,sweep,(s)}$ ((b) and (e) in Figure 1)), and not the bulk values. This is particularly important in cases when the local variations of oxygen partial pressure in the direction normal to the membrane surface are strong, as discussed in Section 2.1. Xu and Thomson [31] assumed that bulk stream parameters (i.e., $P_{O_2,feed,(b)}$ and $P_{O_2,sweep,(b)}$) can approximate the local oxygen partial pressures when they used a similar expression in their numerical and experimental work. Given that measurements of these variations are not often available, we propose to evaluate them using a numerical model, as explained in Section 3. The methodology to compute the oxygen partial pressure profiles is discussed in Section 4. The numerical model makes it possible to evaluate the partial pressures at the membrane

surface, starting with these values in the bulk and the oxygen permeation flux. Using this approach, we recast the oxygen permeation flux in terms of the oxygen partial pressures at the membrane surface, endowing it with wider applicability.

3. OVERALL NUMERICAL MODEL

The analysis of the oxygen transport and fuel conversion processes in an ITM reactor often utilizes a stagnation flow configuration, mostly in the "button-cell" format. A variation on that is shown in Figure 2, showing an experimental apparatus that is under development in our laboratory. This flow configuration was selected because, in the neighborhood of the stagnation line, the profiles of the flow variables including the velocity, temperature, density and species concentrations follow a self-similar solution in the direction normal to the membrane. This simplifies the analysis by reducing the dimensionality of the problem and allows us to implement more complex transport and detailed chemistry models at a manageable computational effort. The membrane divides the physical domain into two computational domains as shown in Figure 2, each governed by a set of equations shown in Section 3.1, coupled through the heat flux and the oxygen permeation flux depending on the partial pressures on both sides. The requisite boundary conditions are discussed in Section 3.2, and finally Section 3.3 discusses the coupling of the air and fuel domains.

3.1. Governing Equations

The governing equations are derived from the general three-dimensional governing equations for reacting flow given by Kee et al. [50]. A low Mach number assumption is imposed because of the low gas velocities, and hence the pressure variations are negligible compared to the thermodynamic pressure, and the oxygen partial pressure is only dependent on its mole fraction. Variations in the z-direction, normal to the $x-y$ plane of the flow, are neglected, where x is measured along the membrane direction and y is the normal direction. A boundary layer approximation is assumed, in which diffusion along the x-direction is neglected with respect to that in the y-direction. Moreover, a self-similar boundary layer solution is sought, in which all the normalized flow variables are function of the direction normal to the membrane and time. The momentum equation in y-direction is therefore decoupled and neglected. Gas-phase radiation is also neglected. The solution variables and the system of governing equations are as follows:

$V(t,y) = \rho\upsilon$: Mass flux (y direction; normal to the membrane) [kg/m^2/s] (13)

$U(t,y) = \frac{u}{x}$: Scaled parallel velocity (x direction; parallel to the membrane) [1/s] (14)

$Y_k(t,y)$: Species mass fraction (15)

$T(t,y)$: Temperature [K] (16)

$\Lambda_x(t) = \frac{1}{x}\frac{dp}{dx}$: Scaled parallel pressure gradient [kg/m^3/s^2] (17)

$$\frac{\partial \rho}{\partial t} + \frac{\partial V}{\partial y} + \alpha\rho U = -\frac{\rho}{T}\frac{\partial T}{\partial t} - \sum_{k=1}^{K}\frac{\rho\bar{W}}{W_k}\frac{\partial Y_k}{\partial t} + \frac{\partial V}{\partial y} + \alpha\rho U = 0$$: Continuity (18)

$$\rho\frac{\partial U}{\partial t} + V\frac{\partial U}{\partial y} + \rho U^2 + \Lambda_x - \frac{\partial}{\partial y}\left(\varphi\frac{\partial U}{\partial y}\right) = 0$$: x-momentum (19)

$$\rho\frac{\partial Y_k}{\partial t} + V\frac{\partial Y_k}{\partial y} + \frac{\partial j_k}{\partial y} - \dot{\omega}_k W_k = 0$$: Species (20)

where, $j_k = -\rho D_{km}\left(\frac{\partial Y_k}{\partial y} + \frac{Y_k}{\bar{W}}\frac{\partial \bar{W}}{\partial y}\right) - \frac{D_k^T}{T}\frac{\partial T}{\partial y}$

$$\rho\frac{\partial T}{\partial t} + V\frac{\partial T}{\partial y} + \frac{1}{c_p}\left[\sum_{k=1}^{K}\hat{h}_k\dot{\omega}_k + \sum_{k=1}^{K}j_k c_{p,k}\frac{\partial T}{\partial y} - \frac{\partial}{\partial y}\left(\lambda\frac{\partial T}{\partial y}\right)\right] = 0$$: Energy (21)

$$\frac{\partial \Lambda_x}{\partial y} = 0$$: Pressure curvature (22)

Where ρ is the density; φ is the dynamic viscosity; D_{km} is the mixture-averaged diffusion coefficient; D_k^T is the thermal diffusion coefficient; $\bar{W}$ is the mixture molecular weight; W_k is the molecular weight of species *k*; $\dot{\omega}_k$ is the molar production rate of species *k*; c_p is the mixture specific heat; $c_{p,k}$ is the specific heat of species *k*; $\hat{h}_k$ is the molar enthalpy of species *k*; λ is the thermal conductivity; K is the number of gas-phase species. Note that α is 1 for a planar configuration and 2 for an axi-symmetric configuration [50]. Along with the system of governing equations, the equation of state is used to compute the density as a function of species mass fractions:

$$\rho = \frac{p\bar{W}}{RT} \tag{23}$$

The pressure curvature equation (22) is added to the system of governing equations to model the finite domain configuration, given that in this case the inlet velocity is imposed as a boundary condition. Thus, the pressure gradient must be determined as a part of the solution. The scaled pressure gradient Λ_x is not a function of y, and is constant throughout the computational domain. Its magnitude is adjusted to satisfy the remaining boundary conditions [50].

The GRI-Mech [51] is implemented to describe the homogeneous gas phase chemical reactions. As nitrogen is not expected to participate in the reactions, the GRI-Mech is reduced to 36 species and 217 reactions. The detailed chemistry enables us to capture important phenomena and chemical species appearing in the neighborhood of the membrane. Cantera [52] is used to integrate the multi-step chemical reactions and evaluate the thermodynamic and the transport properties shown in the governing equations and reaction kinetics using NASA polynomials.

The governing equations and boundary conditions are spatially discretized using finite difference. The diffusion terms in the momentum equation and the species conservation equations are approximated to second-order accuracy. To avoid numerical instabilities [50], the convective terms are discretized with a first-order upwind differencing. The continuity equation is discretized using a first-order fully implicit finite difference. The pressure curvature equation keeps the preconditioner matrix that approximates the inverse of the Jacobian banded. The discretized equations are integrated using the Sundials IDA solver [53], which integrates the differential algebraic equations using a variable-order (from 1 to 5) backward differentiation formula. At each time step, this produces a system of nonlinear algebraic equations, which are solved using a preconditioned Newton-Krylov method.

3.2. Boundary Conditions

The boundary conditions describe inflow conditions at the inlets and flux-matching conditions at the membrane surface. At the inlets, the gas temperature, composition and mass flux are known. Pure normal flow condition implies a zero parallel velocity (i.e., $u_{in} = U_{in} = 0$), and the molar composition of the inflow is determined by that of air ($Y_{k,feed}$)

and a given inlet sweep gas ($Y_{k,sweep}$). The mass influx (V_{feed}, V_{sweep}) and the temperature (T_{feed}, T_{sweep}) are also known. The pressure curvature does not have an explicit boundary condition, and its magnitude is determined to satisfy the mass flux at the inlets. Because the continuity equation is first-order, it needs only one boundary condition at the membrane surface, which is the oxygen permeation rate. The finite-gap stagnation flow configuration requires another mass flux boundary condition at the inlets to account for the given mass influx. This boundary condition is implemented through the pressure curvature equation, in terms of the inlet mass flux boundary condition for continuity. The boundary conditions at the inlets (i.e., $y = H$) can be summarized as,

$$V_{in} = V_{feed},\ V_{sweep} \quad \text{: Pressure curvature} \tag{24}$$

$$U_{in} = 0 \quad \text{: Momentum} \tag{25}$$

$$Y_{k,in} = Y_{k,feed},\ Y_{k,sweep} \quad \text{: Species} \tag{26}$$

$$T_{in} = T_{feed},\ T_{sweep} \quad \text{: Energy} \tag{27}$$

At the membrane surface, flux-matching conditions are applied for the continuity, species and energy conservation equations. Across the ITM, oxygen is transported from the feed side to the permeate side. The convective and diffusive mass fluxes of the gas-phase species at the membrane surface should consider the oxygen permeation rate, J_{O_2}. It is a negative value for the feed side (a sink term), and the permeate side has it as a positive value (source term). Moreover, in the case of a reducing or reactive sweep gas, heat transfer to or from the membrane and the sweep gas is also considered. The energy conservation across the membrane describes the heat flux (Q''_{feed}, Q''_{sweep}) to and from the membrane and its temperature. Note that the oxygen permeation rate and the heat flux are coupling parameters between the feed domain and the permeate domain. The boundary conditions at the membrane surface (i.e., $y = 0$) can be summarized as,

$$V_{mem} = \begin{cases} -J_{O_2} & (feed) \\ +J_{O_2} & (sweep) \end{cases} \quad \text{: Continuity} \tag{28}$$

$$j_k + Y_k V_{mem} = \begin{cases} \pm J_{O_2} & (k = O_2) \\ 0 & (k \neq O_2) \end{cases} \quad \text{: Species} \tag{29}$$

$$Q''_{sweep} - Q''_{feed} - 2\gamma\varepsilon_{mem}\left(T_{mem}^4 - T_\infty^4\right) = 0 \quad \text{: Energy} \tag{30}$$

where, $Q''_{feed} = -\lambda\nabla T + \sum_{k=1}^{K}\left(j_k + Y_k V_{mem}\right)\hat{h}_k$

$$Q''_{sweep} = \lambda\nabla T - \sum_{k=1}^{K}\left(j_k + Y_k V_{mem}\right)\hat{h}_k$$

$$U_{mem} = 0 \quad \text{: Momentum} \tag{31}$$

where γ is the Stefan-Boltzmann constant, T_∞ is the reactor wall temperature, and ε_{mem} is the emissivity of the membrane. Radiation heat transfer may be considered between the membrane and the reactor wall (whose material is Inconel 601). As shown in Figure 2, the membrane sees a large area of the reactor wall, and thus the shape factor is essentially assumed to be one. The emissivity of the membrane, ε_{mem} , is measured at our laboratory, which is approximately 0.8. It is assumed that T_∞ is the same as the gas inlet temperature at steady state. The parallel velocity at the membrane surface (U_{mem}) is set to zero because of the no-slip condition at the solid surface.

3.3. Coupling Computational Domains

The computational domain is divided into two parts, the feed (air) domain and the permeate (sweep gas) domain. The two domains are coupled and the steady state solution is obtained by matching the oxygen permeation flux and the heat flux. Each domain uses the oxygen permeation flux and the heat flux as a flux matching boundary condition at the membrane surface, as stated in expression (28) to (30). Each domain takes into account the permeation flux and the heat flux as given fluxes at the membrane surface during the time integration. After integrating each domain using the inlet boundary conditions and the permeation flux and the heat flux determined during the previous time step, the oxygen partial pressure profile and the temperature profile in each domain are updated. Because the permeation rate depends on the partial pressures of oxygen in both domains, as discussed in Section 2, the new oxygen partial pressures result in an updated oxygen permeation flux for the following time step. Similarly, since the heat flux depends on the temperature profile in both domains, the new temperature profile leads to an updated heat flux for the following time step. This simulation procedure is repeated until the steady state is achieved.

4. PARAMETERIZATION OF SPATIALLY RESOLVED OXYGEN TRANSPORT EXPRESSION

Numerical modeling of reacting flow supported membrane processes requires an oxygen transport flux expression that can be coupled with the gas-phase transport and reaction chemistry in the vicinity of the membrane. This is especially true in the case of oxy-fuel combustion and hydrocarbon reforming. Because of the presence of oxidation reactions near the membrane surface, flow parameters vary significantly throughout the boundary layer on the permeate side. In this case, the bulk stream parameters or mean values (i.e., $P_{O_2,sweep,(b)}$) are substantially different from the local values next to the membrane (i.e., $P_{O_2,sweep,(s)}$) because of the combined transport and chemical reactions. Therefore, the oxygen flux model must be formulated in terms of the local oxygen concentration at the membrane surfaces. These are not available in the literature, and it is difficult to measure these local properties experimentally. Instead, to proceed with our modeling effort, we first use the numerical model of the coupled flow-membrane process described above to derive the parameters in expression (11) and (12) from the measured global values. We use the permeation rates measured by Xu and Thomson. The flux expression in terms of the local oxygen partial pressures is then used to estimate the diffusion coefficient of oxygen vacancies and the reaction rates of surface exchange.

4.1. Estimation of Local Oxygen Partial Pressure

The numerical simulation is used to evaluate the local oxygen partial pressures using the experimentally measured oxygen permeation rates and bulk conditions. To produce the oxygen partial pressure profile, we used the experimentally measured oxygen permeation rates by Xu and Thomson [31]. Using the $La_{0.6}Sr_{0.4}Co_{0.2}Fe_{0.8}O_{3-\delta}$ membrane, they generated 126 data points in a typical disc-type stagnation-flow permeation facility that were used to evaluate the six parameters (pre-exponential factors and activation energies) required in expression (12). Note that they used the bulk stream oxygen partial pressures, $P_{O_2,feed,(b)}$ and $P_{O_2,sweep,(b)}$, measured at the feed air inlet and a sweep gas outlet, respectively. Thus the diffusion coefficient of oxygen vacancies and the reaction rates of surface exchange they derived are evaluated in terms of the bulk stream parameters or mean values. To utilize their permeation rate measurements for a reactive flow supported membrane process, where the parameters in expression (12) should account for the local flow variations, we used our model to numerically reproduce their experiments to determine the local oxygen partial pressures near the membrane surface. As discussed in Section 3.2, the continuity and the species conservation equations need an oxygen permeation rate

to be used as a flux matching boundary condition at the membrane surface. The experimentally measured permeation rates are set as constant boundary conditions (for the continuity and species equations) at the membrane surface such as,

$$V_{mem} = \begin{cases} -J_{O_2,\exp} & (feed) \\ +J_{O_2,\exp} & (sweep) \end{cases} \tag{32}$$

$$j_k + Y_k V_{mem} = \begin{cases} \pm J_{O_2,\exp} & (k = O_2) \\ 0 & (k \neq O_2) \end{cases} \tag{33}$$

where the subscript $\exp$ represents the experimentally measured values.

The corresponding experimental conditions including feed and sweep gas flow rates, molar compositions and membrane temperature are used as boundary conditions at the inlets. Table 1 shows the bulk stream oxygen partial pressures and the membrane temperature at which Xu and Thomson measured oxygen permeation rates. At the feed air inlet, $P_{O_2,feed,(b),\exp}$ is applied as a species boundary condition when the rest of the feed gas is nitrogen.

$$Y_{k,feed} = \begin{cases} \dfrac{P_{O_2,feed,(b),\exp}}{P^{o}} \dfrac{W_{O_2}}{\bar{W}} & (k = O_2) \\ \dfrac{\left(1 - P_{O_2,feed,(b),\exp}\right)}{P^{o}} \dfrac{W_{N_2}}{\bar{W}} & (k = N_2) \\ 0 & (k \neq O_2, N_2) \end{cases} \tag{34}$$

where P^{o} is the operating pressure that is 1 atm. Note that the feed air flow rate is maintained at the maximum value of 150 ml/min (STP) to reduce the gas phase mass transfer effect in the feed domain [31], and thus the mass flux of feed air is,

$$V_{feed} = \frac{150 \rho_{feed}}{A_{feed}} \tag{35}$$

where ρ_{feed} is the density of feed air (STP), and A_{feed} is the feed inlet area of $5.333 \times 10^{-3} m^2$. At the sweep gas inlet, the mass flux of the sweep gas can be found from the measured permeation rates and $P_{O_2,sweep,(b),\exp}$ measured by Xu and Thomson. Since $P_{O_2,sweep,(b),\exp}$ is measured at the sweep gas outlet assuming perfect mixing between the permeated oxygen and the sweep gas, $P_{O_2,sweep,(b),\exp}$ is estimated as,

$$P_{O_2,sweep,(b),\exp} = \frac{J_{O_2,\exp}}{V_{sweep} + J_{O_2,\exp}} \times P^{o} \tag{36}$$

Then, the sweep gas mass flux to be used in the numerical simulations as a sweep gas inlet boundary condition is found by using $P_{O_2,sweep,(b),\exp}$ and the corresponding oxygen permeation rate, $J_{O_2,\exp}$, by rearranging expression (36),

$$V_{sweep} = J_{O_2,\exp}\left(\frac{1}{P_{O_2,sweep,(b),\exp} \Big/ P^{o}} - 1 \right) \tag{37}$$

Nitrogen is used as a sweep gas, and the species boundary condition at the sweep gas inlet is,

$$Y_{k,sweep} = \begin{cases} 1 & (k = N_2) \\ 0 & (k \neq N_2) \end{cases} \tag{38}$$

Both feed air and sweep gases are introduced at the membrane temperature assuming isothermal conditions in the experiments.

$$T_{feed} = T_{sweep} = T_{mem,\exp} \tag{39}$$

By imposing the permeation rate measurements and the corresponding experimental conditions in our numerical model, we computed the local oxygen partial pressures, $P_{O_2,feed,(s)}$ and $P_{O_2,sweep,(s)}$, at each operating condition in Table 1.

4.2. Evaluation of $D_{V_O^{\bullet\bullet}}$, k_f and k_r for Oxygen Transport Expression

The local oxygen partial pressures computed by our numerical model and the membrane temperature are used to evaluate the diffusion coefficient of oxygen vacancies and the surface exchange reaction rates, that is, the six parameters in expression (12) to account for the local flow variations, using a nonlinear regression analysis. $D_{V_O^{\bullet\bullet}}$, k_f and k_r derived from the analysis are shown in Table 2 and Figure 3, where they are compared with the values estimated on the basis of using the bulk stream parameters reported in [31]. The results confirm that the local variations of the oxygen partial pressure should be considered when constructing an oxygen transport model for use in reactive flow studies. The pre-exponential factor, ψ, of the surface exchange reaction rates (k_f and k_r) is substantially larger than that obtained on the basis of using the bulk oxygen partial pressures in the permeation flux. As shown in Figure 1, when the local oxygen concentrations at the surface ((b) and (e) in Figure 1) are considered, the chemical potential gradient is smaller than that determined by the bulk oxygen partial pressures. With respect to activation energy of the surface exchange reaction rates, they remain nearly the same. Because the activation energy accounts primarily for the dependency of the reaction rates on temperature, its magnitude does not vary significantly when the same temperature is used in its evaluation. The pre-exponential factor and the activation energy of the diffusion coefficient also remain essentially the same.

The fact that the coefficients in the oxygen transport expression pertaining to $D_{V_O^{\bullet\bullet}}$, k_f and k_r depend on whether the bulk or the local oxygen partial pressures are used to estimate them highlights the importance of a spatially resolved oxygen partial pressure field and the local oxygen partial pressure in the vicinity of membrane surfaces. The oxygen transport expression should be evaluated by the local oxygen partial pressure. If the oxygen transport expression is based on the oxygen partial pressure at bulk streams as used in previous research, the model cannot predict the oxygen concentration profile in ITM reactors where significant local flow variations exist.

5. FACTORS INFLUENCING OXYGEN TRANSPORT

The numerical model supplemented with the oxygen permeation flux properly parameterized can be used to examine oxygen transport and other processes in membrane supported flows. In typical experimental investigations, the measurement tools are limited and results are shown as function of the bulk stream data which may not be reflective of the local conditions at the membrane surface, especially in the reactive cases. Here we use our spatially resolved model to examine the dependency of the process on different operating parameters including the membrane temperature, feed and sweep gas flow rates, geometry and oxygen concentration in the feed stream. The base-case parameters and the range of their variations in the parametric study are summarized in Table 3. Moreover, the effects of chemical reactions on oxygen transport are discussed. To highlight the importance of local flow variations, the oxygen permeation flux, $J_{O_2,(s)}$, evaluated by the local oxygen partial pressure, $P_{O_2,(s)}$, is compared to that of bulk parameters, $J_{O_2,(b)}$ and $P_{O_2,(b)}$. The spatially resolved numerical model calculates the local oxygen partial pressure, $P_{O_2,(s)}$, and the corresponding permeation rate, $J_{O_2,(s)}$. Next, the bulk oxygen partial pressure, $P_{O_2,(b)}$, is post-processed assuming perfect mixing between the permeated oxygen and the sweep gas, which is the method used in experiments to estimate the permeation rate. By using this bulk oxygen partial pressure, we calculate $J_{O_2,(b)}$.

5.1. Membrane Temperature

The high sensitivity of $D_{V_O^{\bullet\bullet}}$, k_f and k_r to temperature is shown in Figure 3. The resistances of surface exchange kinetics and bulk diffusion to oxygen permeation are reduced significantly with the membrane temperature. According to the lower resistances, the permeation rate increases by nearly four orders of magnitude for a temperature rise from 950K to 1300K, as shown in Figure 4(a). However, beyond a certain point, the sensitivity of oxygen permeation to temperature starts to decrease. This can be explained by the different activation energies of the surface exchange reaction rates and the diffusion coefficient of oxygen vacancies. As shown in Figure 3, the slope of $D_{V_O^{\bullet\bullet}}$ is substantially lower than that of k_f and k_r. As the temperature is raised, the diffusion coefficient of oxygen vacancies becomes limiting factor in oxygen transport [31].

Figure 4(a) shows two different oxygen permeation rates evaluated using the oxygen transport expression based on the oxygen partial pressures at the bulk stream, $J_{O_2,(b)}$, or the local partial pressures at the membrane surface, $J_{O_2,(s)}$, respectively. The figure shows that the dependence on the membrane temperature is weaker when the oxygen permeation rate is described in terms of the local partial pressure. An increasing membrane temperature leads to a larger permeation rate that accounts for a sink and a source term for the feed domain and the permeate domain, respectively. However, the permeation flux and partial pressures are coupled (see Figure 4(b)). The local oxygen partial pressure in the feed side decreases and that of the permeate side increases due to the higher permeation rate, and reduces the chemical potential gradient across the membrane, as shown in Figure 5. We note here that, experimentally, the bulk stream pressure is a mean value measured in the exiting stream. As shown in Figure 5, the oxygen partial pressures change significantly from the membrane surface to the inlet in the permeate domain. Assuming complete mixing in the sweep gas at the exit section, the measured pressure is lower than that at the membrane surface, increasing the apparent partial pressure difference between the two sides and hence not accurately accounting for the dependency of the permeation flux on that parameter.

5.2. Feed and Sweep Gas Flow Rates

Given the significant impact of the gas phase mass transfer on oxygen transport, it is of interest to consider the impacts of the feed and sweep gas flow rates. Figure 6 shows that the permeation rate increases significantly as the sweep gas flow rate is raised. As shown in Figure 6, the spatially averaged parallel velocity on the permeate side increases linearly as the sweep gas flow rate is raised, lowering the oxygen partial pressure. However, the rate of change in the permeation rate and the oxygen partial pressure become smaller as the sweep gas flow rate increases. It can be explained by the spatially resolved partial pressure profiles shown in Figure 7. As the sweep gas flow rate increases, the boundary layer is restricted to a narrow region in the vicinity of the membrane surface. As a result, the oxygen transport becomes less dependent on the sweep gas flow rates.

On the other hand, the permeation rate is much less dependent on the feed gas flow, as shown in Figure 8. At 1100 K (base-case temperature), the forward surface exchange rate, k_f, is higher than both $D_{V_O^{\bullet\bullet}}$ and k_r, as shown in Figure 3, and hence the permeation is limited by the bulk diffusion or the surface exchange kinetics on the permeate side. Thus, although the effects of the gas phase mass transfer in the feed side is reduced by the higher momentum (see Figure 8), the

oxygen permeation rate is hardly affected by an increase in the local oxygen partial pressure. This can also be seen in the spatially resolved partial pressure profiles shown in Figure 9. Whereas the feed side oxygen concentration profiles vary substantially as the feed gas flow rate increases, the oxygen partial pressure in the permeate side does not change, which represents negligible changes in the permeation rate.

Ignoring gas phase mass transfer is valid only at high gas flow rates. As shown in Figure 7, the boundary layer on the permeate side is reduced to a narrow region near the membrane surface when the sweep gas flow rate is raised. In this case, gas phase mass transfer is negligible, and the bulk stream oxygen partial pressure can be used to asymptotically approximate the local oxygen partial pressure (see Figure 6). However, as discussed in Section 2.1.1, the flow rate in ITM reactors is limited by the required stoichiometry of the chemical reactions.

Comparing Figure 4(a) and Figure 6, it can be shown that gains in the permeation rate by increasing the gas flow rates are much smaller than those induced by heating the membrane. The fact that the oxygen permeation rate is weakly dependent on the gas phase flow makes it less efficient to increase the flow rate for enhancing the oxygen permeation rate given that high gas flow rates introduce more pressure drop.

5.3. Geometry – Channel Height from Membrane to Sweep Gas Inlet

To further investigate the dependence of the oxygen permeation rate on the permeate side gas phase mass transfer, a sensitivity analysis with respect to the channel height on the sweep gas side was conducted. A smaller channel height increases the parallel velocity (momentum) on the permeate side reducing the mass transfer effect. In the parametric investigation of the geometry, the sweep gas flow rate is maintained constant. As shown in Figure 10, the local oxygen partial pressure, $P_{O_2,sweep,(s)}$, is lowered with the channel height, enhancing the flux and highlighting the effect of momentum. Note also that the bulk stream parameters ($J_{O_2,(b)}$ and $P_{O_2,sweep,(b)}$) vary in the opposite direction to that of the local flow parameters ($J_{O_2,(s)}$ and $P_{O_2,sweep,(s)}$) with respect to the geometry. Since bulk oxygen partial pressure measured at the exit stream is determined assuming perfect mixing of the permeated oxygen with the sweep gas (refer to expression (36)), its value increases when oxygen permeation is enhanced by reducing the gap height, lowering the apparent bulk stream oxygen partial pressure as opposed to the results based on the local oxygen partial pressures.

5.4. Oxygen Concentration in Feed Air

An increase in the oxygen permeation flux with the oxygen concentration in the feed air is obvious, as discussed in Section 2. In this study, we assume that both feed and permeate domains are at the same operating pressure, which results in no total pressure difference across the ITM, for mechanical stability. The permeation rate J_{O_2} increases when the oxygen partial pressure in the feed air is higher. Note that the effects of gas phase mass transfer in the feed domain are negligible (for the configurations considered in this investigation), as discussed in Section 5.2. Therefore, a larger oxygen partial pressure in the feed air directly increases the local oxygen partial pressure near the membrane surface. Gains in the permeation rate are larger than those induced by the feed gas flow rates, but not as large as those earned by increasing the membrane temperature.

5.5. Chemical Reactions

To capture the effect of chemical reactions on oxygen transport across the membrane, a reactive gas (CH_4) is introduced into the permeate side with diluents (CO_2). Other flow parameters are maintained at the base-case values as listed in Table 3. We note here that to support combustion on the permeate side in the form of a diffusion flame, a substantial amount of oxygen is required. A diffusion flame is established in the region of unity stoichiometry. To achieve a significant oxygen permeation flux for the oxidation reactions, in this study, it is assumed that the feed and sweep gases are introduced at 1300K. Low oxygen concentration due to low permeation would make it necessary to use a higher dilution ratio (for instance CH_4:CO_2 = 1:40 on a molar basis) in order to sustain a diffusion flame. To highlight the impacts of oxidation reactions, the results are compared with those of inert gas.

Oxidation reactions in the permeate side change the oxygen concentration profile as well as the membrane temperature. The oxygen permeation flux increases in reactive environment because oxygen concentration in the permeate side is reduced by consumption in the reaction zone. If the diffusion flame is established in the vicinity of the membrane, the effect of lowering the oxygen concentration is enhanced and the permeation rate increases further. Figure 11 shows that this is indeed the case, and the reaction zone is located a few millimeters away from the membrane. Oxidation reactions in this region reduce the oxygen concentrations compared to the inert gas case, as shown in Figure 12. Furthermore, compared to the inert gas case in which no temperature variations is seen, the membrane in the reactive environment conducts heat

from the permeate to the feed sides. The heat released at the reaction zone is transferred to the membrane, as well as to the feed side, raising its temperature, and further enhancing the oxygen permeation flux. Thus, in a reactive flow, lower oxygen concentration (resulting in $\Delta J_{O_2} = 1.49 \times 10^{-1} \mu mol / cm^2 / s$) and higher membrane temperature (leading to $\Delta J_{O_2} = 1.00 \mu mol / cm^2 / s$) enhance the oxygen permeation flux. In comparison with the inert gas case ($J_{O_2} = 1.15 \mu mol / cm^2 / s$), in the reactive case, the permeation rate is $J_{O_2} = 2.30 \mu mol / cm^2 / s$.

Partial oxidation and fuel pyrolysis are also seen on the permeate side, as reported in [17, 18, 26, 54, 55]. When fuel is introduced into a high temperature reactor without oxygen, the decomposition and pyrolysis of fuel proceed rather than combustion. The oxygen permeation rate and hence the oxygen concentration on the permeate side are rather low, resulting in a fuel-rich environment in the reaction zone. In this case, instead of being fully converted to carbon dioxide (complete combustion), methane is partially oxidized to form synthesis gas composed of carbon monoxide and hydrogen, as follows.

$$CH_4 + \frac{1}{2} O_2 \rightarrow CO + 2H_2 \tag{40}$$

Figure 13(a) shows the spatially resolved species concentrations. Within the reaction zone, fuel-rich conditions are established, and the partial oxidation of fuel produces carbon monoxide and hydrogen. Note that the fuel stream is highly diluted by carbon dioxide. Methane is reformed to produce carbon monoxide and hydrogen by carbon dioxide reforming reaction as shown below.

$$CH_4 + CO_2 \rightarrow 2CO + 2H_2 \tag{41}$$

Moreover, methane is decomposed and pyrolyzed before reaching the reaction front at 1300K, as shown in Figure 13(b). Fuel pyrolysis may result in soot formation and carbon deposition on the membrane surface [56]. Deposited carbon degrades the membrane activity including oxygen permeation. Rigorous investigation on these phenomena will be conducted using the current model. The location of the reaction zone along with fuel pyrolysis shows the importance of

possible heterogeneous reactions on the membrane surface [57]. It has been reported that typical mixed-conducing ion transport membranes exhibit catalytic activities [29]. This is another phenomenon that will be investigated in a subsequent work.

6. CONCLUSIONS

A numerical model for oxygen transport and fuel conversion processes in an ITM reactor was presented. The model is consistent with a finite-gap stagnation flow configuration, which is often used in experimental studies. The membrane separates the domain into two sides, the feed side and the permeate side, coupled by the oxygen permeation flux and the heat flux across the membrane. The model is based on the transport of mass, momentum and energy on both sides while imposing appropriate boundary conditions, and accounting for detailed transport and chemistry. We have implemented an efficient numerical approach to obtain solutions over a wide range of operating conditions.

First, we used available experimental data and the numerical model to obtain an expression for the oxygen permeation flux in terms of the oxygen partial pressure at the membrane surface on both sides. We demonstrated that this is a more accurate and general representation that allows the application of the resulting expression over a wider range of conditions. We showed that neglecting the impact of mass transfer in parameterizing the dependency of the permeation flux on the operating conditions may lead to errors. The flux expression accounts for the adsorption/desorption kinetics and the diffusion across the membrane. The values of the parameters $D_{v_O^{\bullet\bullet}}$, k_f and k_r evaluated using the local oxygen partial pressures confirm that the local variations should be considered when constructing an oxygen transport model.

The resulting model was then used to examine the impact of the operating conditions, such as the membrane temperature, feed and sweep gas flow rates, geometry, oxygen concentration in the feed air and chemical reactions on oxygen transport. The oxygen permeation rate depends most strongly on the membrane temperature, but also on the gas flow rates and the channel height on the permeate side. Moreover, a lower oxygen concentration in the permeate side and a higher membrane temperature resulting from fuel oxidation reactions on the permeate side enhance the oxygen permeation rate. A reaction zone located in the vicinity of the membrane consumes the permeated oxygen and reduces its partial

pressure. A high temperature and low oxygen concentration environment may also result in the partial oxidation and/or the pyrolysis of fuel. The latter is a subject of current studies.

7. ACKNOWLEDGEMENTS

The authors would like to thank the King Fahd University of Petroleum and Minerals (KFUPM) in Dharan, Saudi Arabia, for funding the research reported in this paper through the Center of Clean Water and Clean Energy at Massachusetts Institute of Technology and KFUPM. This work is also supported by King Abdullah University of Science and Technology grant number KSU-I1-010-01.

8. NOMENCLATURE

P_{O_2}	Oxygen partial pressure
J_{O_2}	Oxygen permeation rate
$V_O^{\bullet\bullet}$	Oxygen vacancy
O_o^x	Lattice oxygen ion
$h^{\bullet}$	Electron hole
μ_i	Chemical potential of species *i*
k_i	Surface exchange rate of reaction *i*
J_i	Permeation rate of charged defects *i*
C_i	Molar concentration of charged defects *i*
σ_i	Ionic conductivity of charged defects *i*
z_i	Charge number of charged defects *i*
η_i	Electrochemical potential of charged defects *i*
D_i	Diffusivity of charged defects *i*

ϕ	Electric potential
F	Faraday constant
ξ	Transmission coefficient
κ_B	Boltzmann constant
h_p	Planck constant
E_A	Activation energy
ψ	Pre-exponential factor
L	Membrane thickness
R	Universal gas constant
V	Mass flux
U	Scaled parallel velocity
Y_k	Mass fraction of gas-phase species *k*
T	Temperature
Λ_x	Scaled parallel pressure gradient
ρ	Density
φ	Dynamic viscosity
D_{km}	Mixture-averaged diffusion coefficient
D_k^T	Thermal diffusion coefficient
$\bar{W}$	Mixture molecular weight
W_k	Molecular weight of species *k*
$\dot{\omega}_k$	Molar production rate of species *k*
c_p	Mixture specific heat
$c_{p,k}$	Specific heat of species *k*
$\hat{h}_k$	Molar enthalpy of species *k*

λ	Thermal conductivity
K	Number of gas-phase species
ε	Emissivity
H	Channel height from membrane to inlet
γ	Stefan-Boltzmann constant
P^{o}	Operating pressure
A	Area

subscripts

feed	Feed side of membrane
sweep	Sweep gas (permeate) side of membrane
in	Inlet
mem	Membrane
exp	Experimentally measured values
(s)	Membrane surface
(b)	Bulk stream
∞	Reactor wall

9. REFERENCES

1. A. Leo, S. Liu, J.C. Diniz da Costa, *Development of mixed conducting membranes for clean coal energy delivery,* International Journal of Greenhouse Gas Control, **3** (4) (2009) 357-367.
2. R. Bredesen, K. Jordal, O. Bolland, *High-temperature membranes in power generation with CO_2 capture,* Chemical Engineering and Processing, **43** (9) (2004) 1129-1158.
3. B. Cales, J.F. Baumard, *Oxygen semipermeability and electronic conductivity in calcia-stabilized zirconia,* Journal of Materials Science, **17** (11) (1982) 3243-3248.
4. B. Cales, J.F. Baumard, *Mixed conduction and defect structure of ZrO_2-CeO_2-Y_2O_3 solid solutions,* Journal of the Electrochemical Society, **131** (10) (1984) 2407-2413.
5. Y. Teraoka, H.M. Zhang, S. Furukawa, N. Yamazoe, *Oxygen permeation through perovskite-type oxides,* Chemistry Letters, **11** (1985) 1743-1746.
6. Y. Teraoka, H.M. Zhang, S. Furukawa, N. Yamazoe, *Mixed ionic-electronic conductivity of $La_{1-x}Sr_xCo_{1-y}Fe_yO_{3-\delta}$ perovskite-type oxides,* Materials Research Bulletin, **23** (1) (1988) 51-58.
7. S. Diethelm, J. Van herle, P.H. Middleton, D. Favrat, *Oxygen permeation and stability of $La_{0.4}Ca_{0.6}Fe_{1-x}Co_xO_{3-\delta}$ (x = 0, 0.25, 0.5) membranes,* Journal of Power Sources, **118** (1-2) (2003) 270-275.

8. Z. Shao, G. Xiong, Y. Cong, W. Yang, *Synthesis and oxygen permeation study of novel perovskite-type $BaBi_xCo_{0.2}Fe_{0.8-x}O_{3-\delta}$ ceramic membranes,* Journal of Membrane Science, **164** (1-2) (1999) 167-176.
9. J. Tong, W. Yang, R. Cai, B. Zhu, G. Xiong, L. Lin, *Investigation on the structure stability and oxygen permeability of titanium-doped perovskite-type oxides of $BaTi_{0.2}Co_xFe_{0.8-x}O_{3-\delta}$ (x = 0.2~0.6),* Separation and Purification Technology, **32** (1-3) (2003) 289-299.
10. H. Wang, Y. Cong, W. Yang, *Oxygen permeation study in a tubular $Ba_{0.5}Sr_{0.5}Co_{0.8}Fe_{0.2}O_{3-\delta}$ oxygen permeable membrane,* Journal of Membrane Science, **210** (2) (2002) 259-271.
11. W. Ito., T. Nagai, T. Sakon, *Oxygen separation from compressed air using a mixed conducting perovskite-type oxide membrane,* Solid State Ionics, **178** (11-12) (2007) 809-816.
12. S. Liu, G.R. Gavalas, *Oxygen selective ceramic hollow fiber membranes,* Journal of Membrane Science, **246** (1) (2004) 103-108.
13. C. Tablet, G. Grubert, H. Wang, T. Schiestel, M. Schroeder, B. Langanke, J. Caro, *Oxygen permeation study of perovskite hollow fiber membranes,* Catalysis Today, **104** (2-4) (2005) 126-130.
14. Y. Zeng, Y.S. Lin, S.L. Swartz, *Perovskite-type ceramic membrane: synthesis, oxygen permeation and membrane reactor performance for oxidative coupling of methane,* Journal of Membrane Science, **150** (1) (1998) 87-98.
15. W. Jin, S. Li, P. Huang, N. Xu, J. Shi, Y.S. Lin, *Tubular lanthanum cobaltite perovskite-type membrane reactors for partial oxidation of methane to syngas,* Journal of Membrane Science, **166** (1) (2000) 13-22.
16. S.J. Xu, W.J. Thomson, *Stability of $La_{0.6}Sr_{0.4}Co_{0.2}Fe_{0.8}O_{3-\delta}$ perovskite membranes in reducing and nonreducing environments,* Industrial & Engineering Chemistry Research, **37** (4) (1998) 1290-1299.
17. M. Ikeguchi, T. Mimura, Y. Sekine, E. Kikuchi, M. Matsukata, *Reaction and oxygen permeation studies in $Sm_{0.4}Ba_{0.6}Fe_{0.8}Co_{0.2}O_{3-\delta}$ membrane reactor for partial oxidation of methane to syngas,* Applied Catalysis A: General, **290** (1-2) (2005) 212-220.
18. C. Tsai, A.G. Dixon, W.R. Moser, Y.H. Ma, *Dense perovskite membrane reactors for partial oxidation of methane to syngas,* AlChE, **43** (11A) (1997) 2741-2750.
19. G. Saracco, H.W.J.P. Neomagus, G.F. Versteeg, W.P.M. van Swaaij, *High-temperature membrane reactors: potential and problems,* Chemical Engineering Science, **54** (13-14) (1999) 1997-2017.
20. S. Engels, F. Beggel, M. Modigell, H. Stadler, *Simulation of a membrane unit for oxyfuel power plants under consideration of realistic BSCF membrane properties,* Journal of Membrane Science, **359** (1-2) (2010) 93-101.
21. X. Tan, K. Li, A. Thursfield, I.S. Metcalfe, *Oxyfuel combustion using a catalytic ceramic membrane reactor,* Catalysis Today, **131** (1-4) (2008) 292-304.
22. H.J.M. Bouwmeester, *Dense ceramic membranes for methane conversion,* Catalysis Today, **82** (1-4) (2003) 141-150.
23. P.N. Dyer, R.E. Richards, S.L. Russek, D.M. Taylor, *Ion transport membrane technology for oxygen separation and syngas production,* Solid State Ionics, **134** (1-2) (2000) 21-33.
24. J. Smit, W. Zhang, v.S. Annaland, J.A.M. Kuipers, *Feasibility study of a novel membrane reactor for syngas production, Part 2: Adiabatic reactor simulations,* Journal of Membrane Science, **291** (1-2) (2007) 33-45.
25. X. Tan, K. Li, *Design of mixed conducting ceramic membranes/reactors for the partial oxidation of methane to syngas,* AlChE, **55** (10) (2009) 2675-2685.
26. U. Balachandran, J.T. Dusek, R.L. Mieville, R.B. Poeppel, M.S. Kleefisch, S. Pei, T.P. Kobylinski, C.A. Udovich, A.C. Bose, *Dense ceramic membranes for partial oxidation of methane to syngas,* Applied Catalysis, **133** (1) (1995) 19-29.
27. W. Wang, Y.S. Lin, *Analysis of oxidative coupling of methane in dense oxide membrane reactors,* Journal of Membrane Science, **103** (3) (1995) 219-233.
28. J.E. ten Elshof, H.J.M. Bouwmeester, H. Verweij, *Oxidative coupling of methane in a mixed-conducting perovskite membrane reactor,* Applied Catalysis, **130** (2) (1995) 195-212.
29. A. Julbe, D. Farrusseng, C. Guizard, *Limitations and potentials of oxygen transport dense and porous ceramic membranes for oxidation reactions,* Catalysis Today, **104** (2-4) (2005) 102-113.
30. W. Jin, X. Gu, S. Li, P. Huang, N. Xu, J. Shi, *Experimental and simulation study on a catalyst packed tubular dense membrane reactor for partial oxidation of methane to syngas,* Chemical Engineering Science, **55** (14) (2000) 2617-2625.
31. S.J. Xu, W.J. Thomson, *Oxygen permeation rate through ion-conducting perovskite membranes,* Chemical Engineering Science, **54** (17) (1999) 3839-3850.
32. H.J.M. Bouwmeester, A.J. Burggraaf. *Chapter 10: Dense ceramic membranes for oxygen separation*, in *Fundamentals of inorganic membrane science and technology*. Burggraaf, A.J. and Cot, L., Editors. 1996, Elsevier.

33. B.A. van Hassel, *Oxygen transfer across composite oxygen transport membranes,* Solid State Ionics, **174** (1-4) (2004) 253-260.
34. P.S. Manning, J.D. Sirman, J.A. Kilner, *Oxygen self-diffusion and surface exchange studies of oxide electrolytes having the fluorite structure,* Solid State Ionics, **93** (1-2) (1996) 125-132.
35. T. Ishihara, J.A. Kilner, M. Honda, N. Sakai, Y. Harumi, T. Yusaku, *Oxygen surface exchange and diffusion in $LaGaO_3$ based perovskite type oxides,* Solid State Ionics, **113-115** (1998) 593-600.
36. E. Ruiz-Trejo, J.D. Sirman, Y.M. Baikov, J.A. Kilner, *Oxygen ion diffusivity, surface exchange and ionic conductivity in single crystal Gadolinia doped Ceria,* Solid State Ionics, **113-115** (1998) 565-569.
37. J.A. Lane, J.A. Kilner, *Oxygen surface exchange on Gadolinia doped Ceria,* Solid State Ionics, **136-137** (2000) 927-932.
38. J.M. Gozalvez-Zafrilla, A. Santafe-Moros, S. Escolastico, J.M. Serra, *Fluid dynamic modeling of oxygen permeation through mixed ionic-electronic conducting membranes,* Journal of Membrane Science, **378** (1-2) (2011) 290-300.
39. J. Fleig, *On the current-voltage characteristics of charge transfer reactions at mixed conducting electrodes on solid electrolytes,* Physical Chemistry Chemical Physics, **7** (2005) 2027-2037.
40. D.S. Mebane, M. Liu, *Classical, phenomenological analysis of the kinetics of reactions at the gas-exposed surface of mixed ionic electronic conductors,* Journal of Solid State Electrochemistry, **10** (8) (2006) 575-580.
41. Y.S. Lin, W. Wang, J. Han, *Oxygen permeation through thin mixed-conducting solid oxide membranes,* AlChE, **40** (5) (1994) 786-798.
42. B.A. van Hassel, T. Kawada, N. Sakai, H. Yokokawa, M. Dokiya, H.J.M. Bouwmeester, *Oxygen permeation modelling of perovskites,* Solid State Ionics, **66** (3-4) (1993) 295-305.
43. H.J.M. Bouwmeester, H. Kruidhof, A.J. Burggraaf, *Importance of the surface exchange kinetics as rate limiting step in oxygen permeation through mixed-conducting oxides,* Solid State Ionics, **72** (2) (1994) 185-194.
44. S. Dou, C.R. Masson, P.D. Pacey, *Mechanism of oxygen permeation through lime-stabilized Zirconia,* Journal of Electrochemical Society, **132** (8) (1985) 1843-1849.
45. Y. Liu, X. Tan, K. Li, *Mixed conducting ceramics for catalytic membrane processing,* Catalysis Reviews, **48** (2) (2006) 145-198.
46. S. Kim, Y.L. Yang, A.J. Jacobson, B. Abeles, *Diffusion and surface exchange coefficients in mixed ionic electronic conducting oxides from the pressure dependence of oxygen permeation,* Solid State Ionics, **106** (3-4) (1998) 189-195.
47. L. Qiu, T.H. Lee, L.M. Liu, Y.L. Yang, A.J. Jacobson, *Oxygen permeation studies of $SrCo_{0.8}Fe_{0.2}O_{3-\delta}$,* Solid State Ionics, **76** (3-4) (1995) 321-329.
48. X. Qi, Y.S. Lin, S.L. Swartz, *Electric transport and oxygen permeation properties of Lanthanum Cobaltite membranes synthesized by different methods,* Industrial & Engineering Chemistry Research, **39** (3) (2000) 646-653.
49. Z. Yang, Y.S. Lin, *A semi-empirical equation for oxgyen nonstoichiometry of perovskite-type ceramics,* Solid State Ionics, **150** (3-4) (2002) 242-254.
50. R.J. Kee, M.E. Coltrin, P. Glarborg, *Chemically Reacting Flow: Theory & Practice*, Wiley-Interscience, 2003.
51. G.P. Smith, D.M. Golden, M. Frenklach, N.W. Moriarty, B. Eiteneer, M. Goldenberg, C.T. Bowman, R.K. Hanson, S. Song, W.C. Gardiner, V.V. Lissianski, Z. Qin. *GRI-Mech 3.0*. Available from: http://www.me.berkeley.edu/gri_mech/.
52. D.G. Goodwin. *Cantera*. Available from: http://www.aresinstitute.org/Cantera/cantera-cxx.pdf.
53. Lawrence-Livermore-National-Laboratory. *SUite of Nonlinear and DIfferential ALgebraic equation Solvers (SUNDIALS)*, https://computation.llnl.gov/casc/sundials/main.html.
54. W. Zhang, J. Smit, v.S. Annaland, J.A.M. Kuipers, *Feasibility study of a novel membrane reactor for syngas production, Part 1: Experimental study of O_2 permeation through perovskite membranes under reducing and non-reducing atmospheres,* Journal of Membrane Science, **291** (1-2) (2007) 19-32.
55. C.J. Sung, J.B. Liu, C.K. Law, *Structural response of counterflow diffusion flames to strain rate variations,* Combustion and Flame, **102** (4) (1995) 481-492.
56. J.R. Anderson, M. Boudart, *Catalysis: Science and Technology*, ed. Springer-Verlag. Vol. 5, Berlin, 1984.
57. J.G. McCarty, H. Wise, *Perovskite catalysts for methane combustion,* Catalysis Today, **8** (2) (1990) 231-248.

List of Figures

FIGURE 1 OXYGEN TRANSPORT PROCESSES WITHIN THE ITM UNIT FOLLOWING THE OXYGEN CHEMICAL POTENTIAL GRADIENT (REVISED FROM [1])

FIGURE 2 FINITE-GAP STAGNATION FLOW CONFIGURATION CONSIDERED IN THIS INVESTIGATION (FEED INLET AREA = $A_{feed} = 5.333 \times 10^{-3} m^2$, SWEEP GAS INLET AREA = A_{sweep} = MEMBRANE AREA = $A_{mem} = 5.806 \times 10^{-3} m^2$, H_{feed} AND H_{sweep} ARE VARIABLES)

FIGURE 3 THE VARIATIONS OF THE DIFFUSION COEFFICIENT OF OXYGEN VACANCIES AND THE REACTION RATES OF SURFACE EXCHANGE WITH CHANGES IN THE MEMBRANE TEMPERATURE ($D_{V_O^{\bullet\bullet},(s)}, k_{f,(s)}, k_{r,(s)}$ COMPUTED BY $P_{O_2,(s)}$ USING THE NUMERICAL MODEL AND $D_{V_O^{\bullet\bullet},(b)}, k_{f,(b)}, k_{r,(b)}$ ESTIMATED BY $P_{O_2,(b),\exp}$ REPORTED IN [31])

FIGURE 4 INFLUENCES OF MEMBRANE TEMPERATURE ON: (A) THE OXYGEN PERMEATION RATE AND (B) THE OXYGEN PARTIAL PRESSURE ($V_{feed} = 0.1 kg/m^2/s$, $V_{sweep} = 0.1 kg/m^2/s$, $H_{feed} = 50.8 mm$, $H_{sweep} = 25.4 mm$, $L = 1.0 mm$)

FIGURE 5 SPATIALLY RESOLVED OXYGEN PARTIAL PRESSURE PROFILES AS A FUNCTION OF THE MEMBRANE TEMPERATURE ($V_{feed} = 0.1 kg/m^2/s$, $V_{sweep} = 0.1 kg/m^2/s$, $H_{feed} = 50.8 mm$, $H_{sweep} = 25.4 mm$, $L = 1.0 mm$)

FIGURE 6 THE EFFECTS OF SWEEP GAS FLOW RATE ON THE OXYGEN PERMEATION RATE, THE OXYGEN PARTIAL PRESSURE ON THE SWEEP GAS SIDE AND THE SPATIALLY AVERAGED PARALLEL VELOCITY ON THE SWEEP GAS SIDE, $U_{sweep,avg} = \frac{1}{H_{sweep}} \int_0^{H_{sweep}} U_{sweep}(t,y) dy$ ($V_{feed} = 0.1 kg/m^2/s$, $T_{mem} = 1100 K$, $H_{feed} = 50.8 mm$, $H_{sweep} = 25.4 mm$, $L = 1.0 mm$)

FIGURE 7 SPATIALLY RESOLVED OXYGEN PARTIAL PRESSURE PROFILES AS A FUNCTION OF THE SWEEP GAS FLOW RATE ($V_{feed} = 0.1 kg/m^2/s$, $T_{mem} = 1100 K$, $H_{feed} = 50.8 mm$, $H_{sweep} = 25.4 mm$, $L = 1.0 mm$)

FIGURE 8 THE EFFECTS OF FEED AIR FLOW RATE ON THE OXYGEN PERMEATION RATE, THE OXYGEN PARTIAL PRESSURE ON THE FEED SIDE AND THE SPATIALLY AVERAGED PARALLEL VELOCITY ON THE FEED SIDE, $U_{feed,avg} = \frac{1}{H_{feed}} \int_0^{H_{feed}} U_{feed}(t,y) dy$ ($V_{sweep} = 0.1 kg/m^2/s$, $T_{mem} = 1100 K$, $H_{feed} = 50.8 mm$, $H_{sweep} = 25.4 mm$, $L = 1.0 mm$)

FIGURE 9 SPATIALLY RESOLVED OXYGEN PARTIAL PRESSURE PROFILES AS A FUNCTION OF THE FEED AIR FLOW RATE ($V_{sweep} = 0.1 kg/m^2/s$, $T_{mem} = 1100 K$, $H_{feed} = 50.8 mm$, $H_{sweep} = 25.4 mm$, $L = 1.0 mm$)

FIGURE 10 THE EFFECTS OF GEOMETRY (CHANNEL HEIGHT FROM THE MEMBRANE TO THE SWEEP GAS INLET) ON THE OXYGEN PERMEATION RATE, THE OXYGEN PARTIAL PRESSURE ON THE SWEEP GAS SIDE AND THE SPATIALLY AVERAGED PARALLEL VELOCITY, $U_{sweep,avg} = \frac{1}{H_{sweep}} \int_0^{H_{sweep}} U_{sweep}(t,y) dy$ ($V_{feed} = 0.1 kg/m^2/s$, $V_{sweep} = 0.1 kg/m^2/s$, $T_{mem} = 1100 K$, $H_{feed} = 50.8 mm$, $L = 1.0 mm$)

FIGURE 11 TEMPERATURE VARIATIONS WHEN SWEEP GAS IS INERT GAS OR REACTIVE GAS ($V_{feed} = 0.1 kg/m^2/s$, $V_{sweep} = 0.1 kg/m^2/s$, $T_{in} = 1300 K$, $H_{feed} = 50.8 mm$, $H_{sweep} = 25.4 mm$, $L = 1.0 mm$)

FIGURE 12 SPATIALLY RESOLVED OXYGEN PARTIAL PRESSURE PROFILES WHEN SWEEP GAS IS INERT GAS OR REACTIVE GAS ($V_{feed} = 0.1 kg/m^2/s$, $V_{sweep} = 0.1 kg/m^2/s$, $T_{in} = 1300 K$, $H_{feed} = 50.8 mm$, $H_{sweep} = 25.4 mm$, $L = 1.0 mm$)

FIGURE 13 INFLUENCES OF CHEMICAL REACTIONS ON THE SPECIES CONCENTRATION VARIATIONS WHEN A REACTIVE GAS IS USED AS A SWEEP GAS: (A) MAJOR SPECIES INCLUDING CH_4, O_2, CO, H_2, AND H_2O, AND (B) SOOT PRECURSORS INCLUDING C_2H_2 AND C_2H_4 ($V_{feed} = 0.1 kg/m^2/s$, $V_{sweep} = 0.1 kg/m^2/s$, $T_{in} = 1300 K$, $H_{feed} = 50.8 mm$, $H_{sweep} = 25.4 mm$, $L = 1.0 mm$)

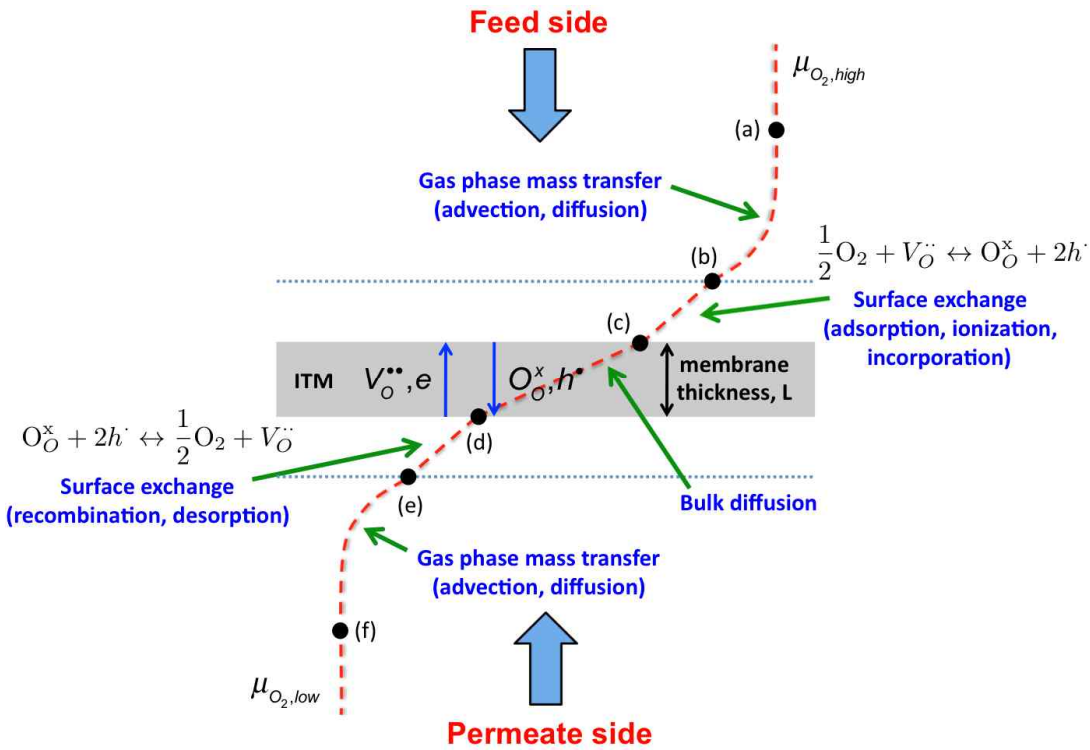

Figure 1 Oxygen transport processes within the ITM unit following the oxygen chemical potential gradient (revised from [1])

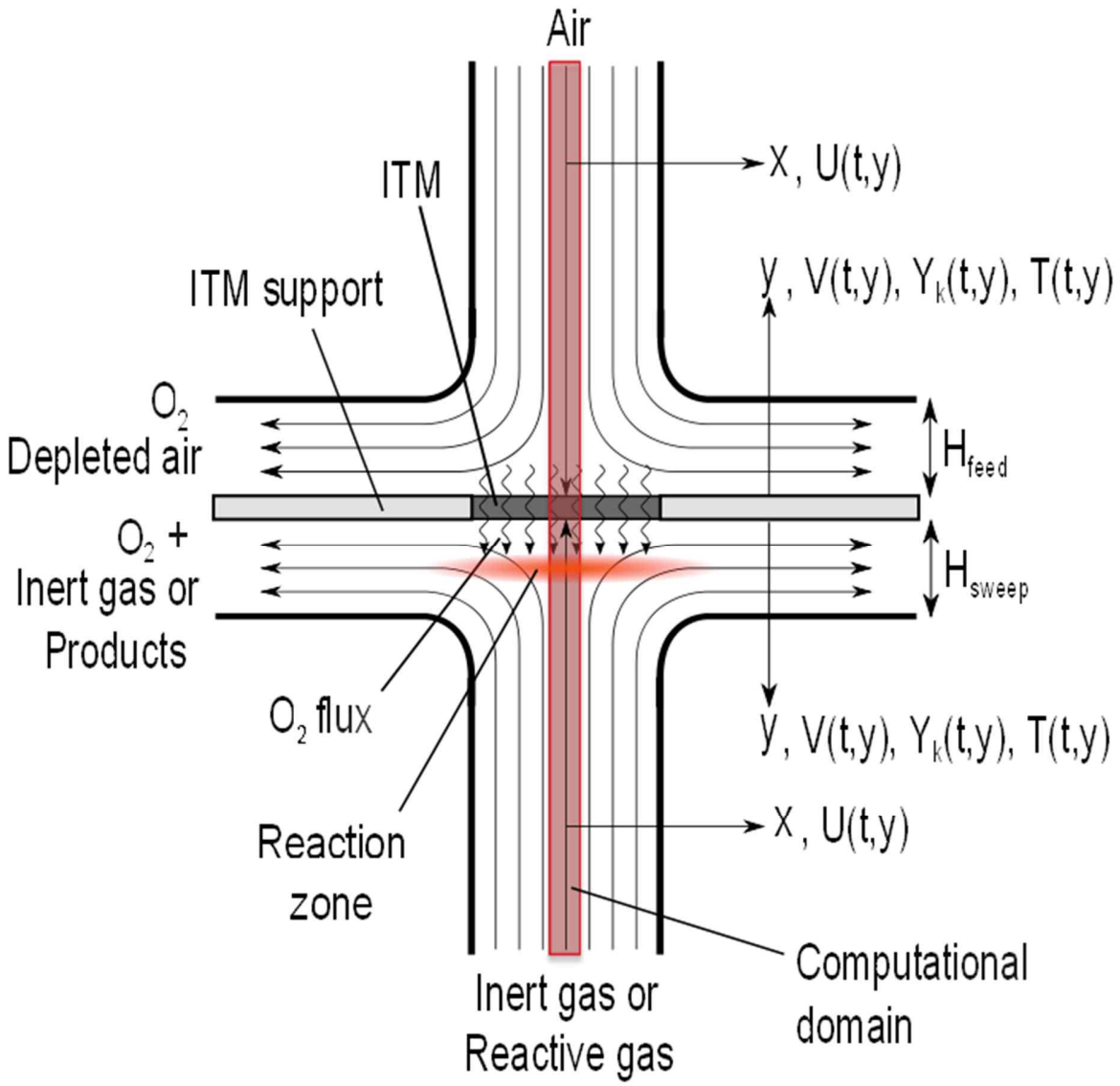

Figure 2 Finite-gap stagnation flow configuration considered in this investigation (feed inlet area = $A_{feed} = 5.333 \times 10^{-3} m^2$, sweep gas inlet area = A_{sweep} = membrane area = $A_{mem} = 5.806 \times 10^{-3} m^2$, H_{feed} and H_{sweep} are variables)

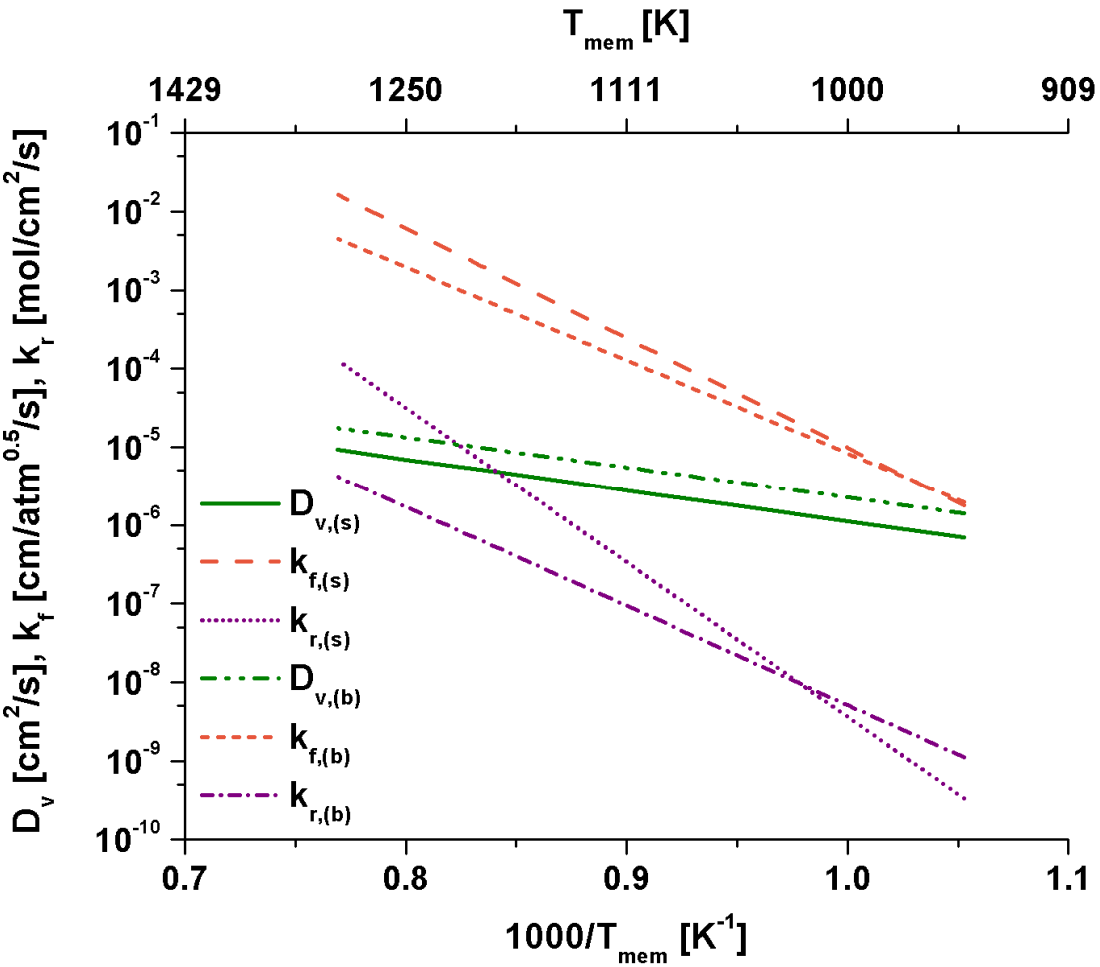

Figure 3 The variations of the diffusion coefficient of oxygen vacancies and the reaction rates of surface exchange with changes in the membrane temperature ($D_{V_O^{\bullet\bullet},(s)}, k_{f,(s)}, k_{r,(s)}$ computed by $P_{O_2,(s)}$ using the numerical model and $D_{V_O^{\bullet\bullet},(b)}, k_{f,(b)}, k_{r,(b)}$ estimated by $P_{O_2,(b),\exp}$ reported in [31])

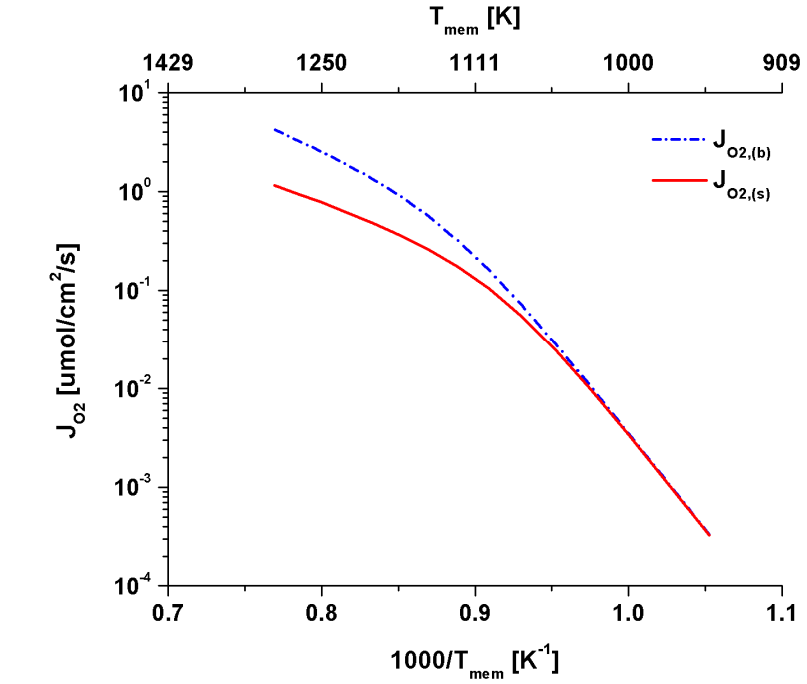

(a)

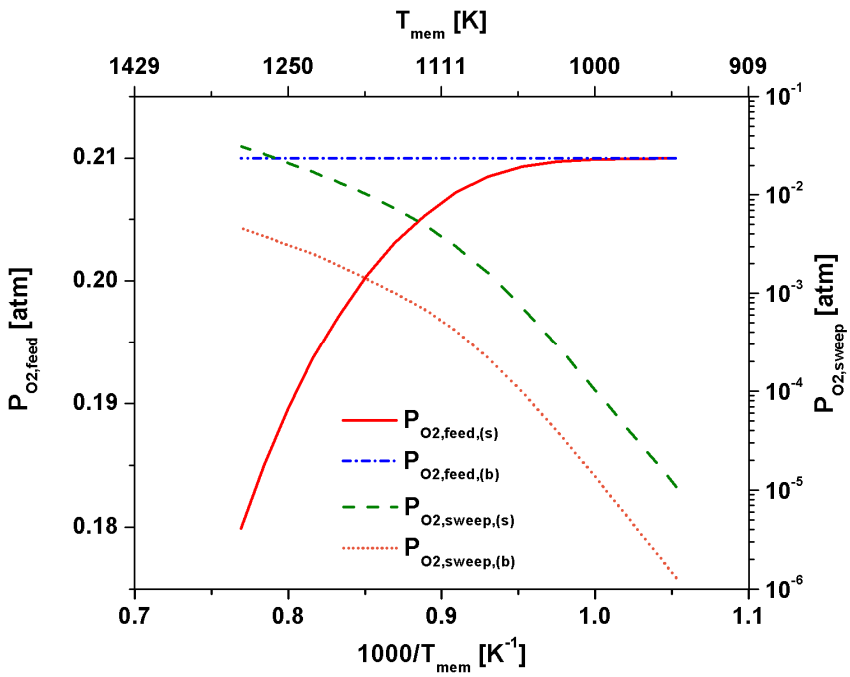

(b)

Figure 4 Influences of membrane temperature on: (a) the oxygen permeation rate and (b) the oxygen partial pressure ($V_{feed} = 0.1kg/m^2/s$, $V_{sweep} = 0.1kg/m^2/s$, $H_{feed} = 50.8mm$, $H_{sweep} = 25.4mm$, $L = 1.0mm$ **)**

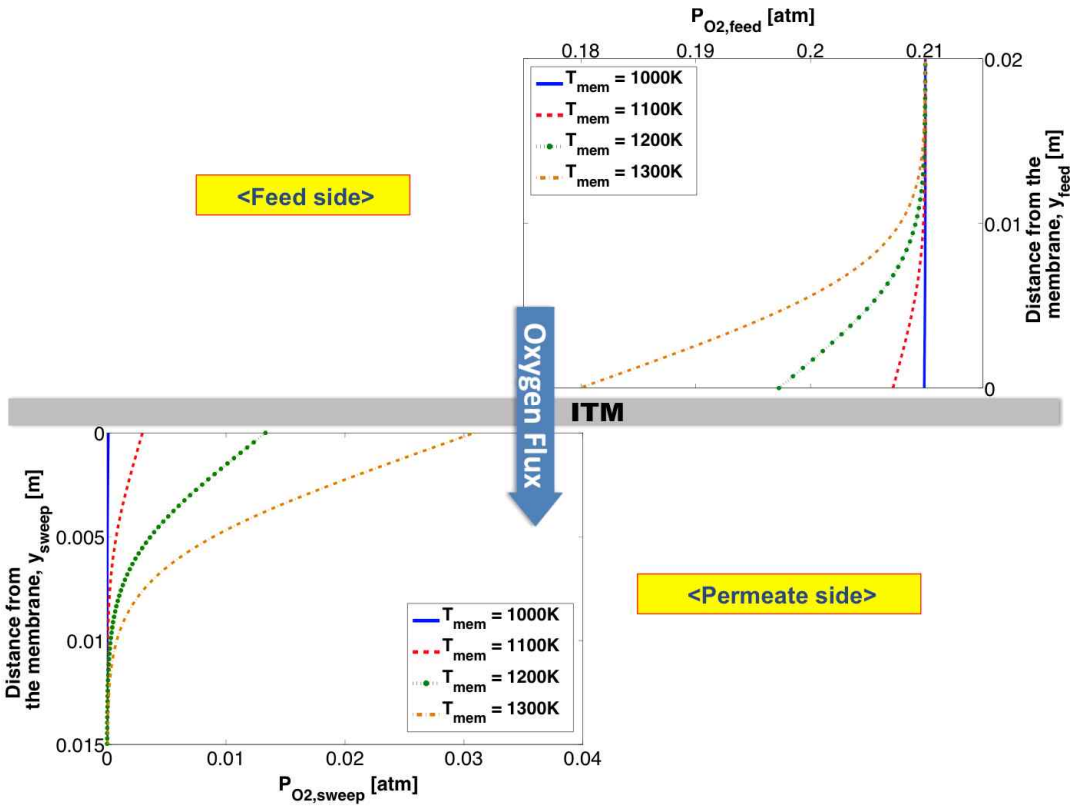

Figure 5 Spatially resolved oxygen partial pressure profiles as a function of the membrane temperature ($V_{feed} = 0.1kg/m^2/s$, $V_{sweep} = 0.1kg/m^2/s$, $H_{feed} = 50.8mm$, $H_{sweep} = 25.4mm$, $L = 1.0mm$)

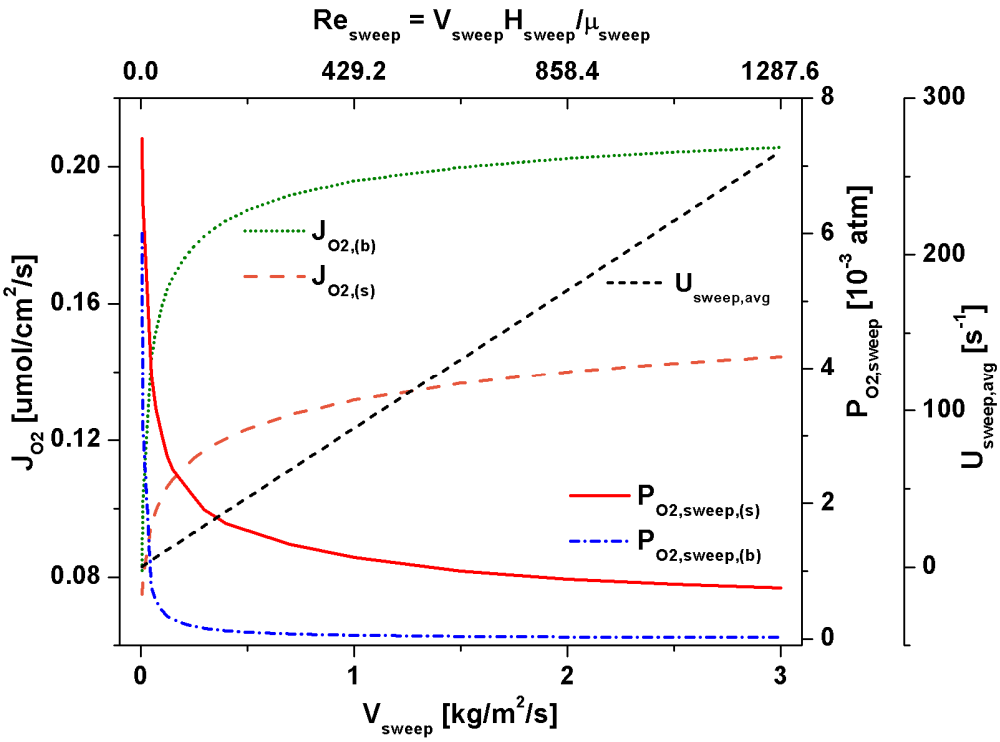

Figure 6 The effects of sweep gas flow rate on the oxygen permeation rate, the oxygen partial pressure on the sweep gas side and the spatially averaged parallel velocity on the sweep gas side, $U_{sweep,avg} = \frac{1}{H_{sweep}} \int_0^{H_{sweep}} U_{sweep}(t,y)dy$

$(V_{feed} = 0.1kg/m^2/s,\ T_{mem} = 1100K,\ H_{feed} = 50.8mm,\ H_{sweep} = 25.4mm,\ L = 1.0mm)$

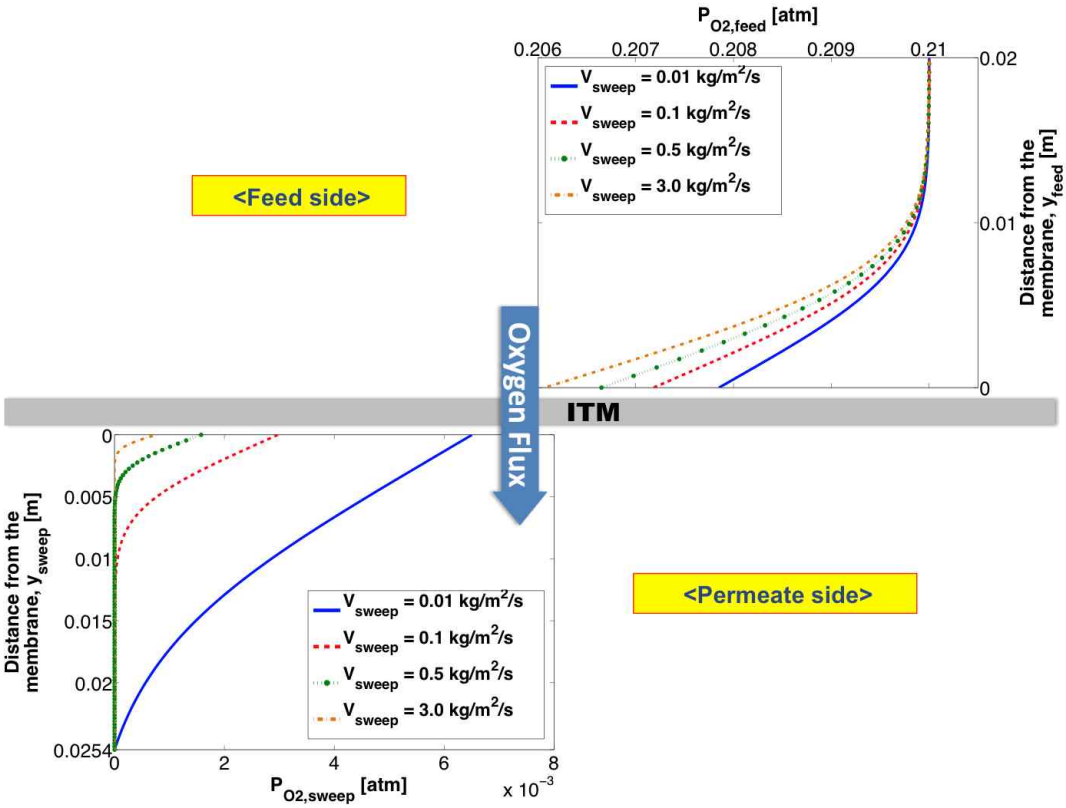

Figure 7 Spatially resolved oxygen partial pressure profiles as a function of the sweep gas flow rate ($V_{feed} = 0.1kg/m^2/s$, $T_{mem} = 1100K$, $H_{feed} = 50.8mm$, $H_{sweep} = 25.4mm$, $L = 1.0mm$)

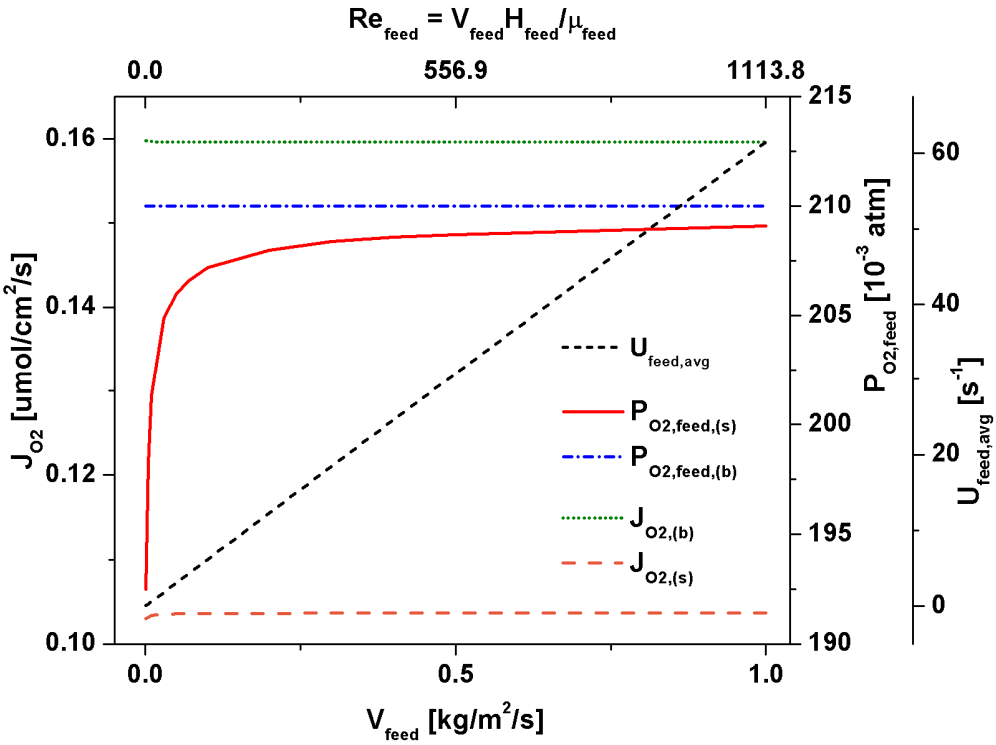

Figure 8 The effects of feed air flow rate on the oxygen permeation rate, the oxygen partial pressure on the feed side and the spatially averaged parallel velocity on the feed side, $U_{feed,avg} = \frac{1}{H_{feed}} \int_0^{H_{feed}} U_{feed}(t,y)dy$

$(V_{sweep} = 0.1kg/m^2/s,\ T_{mem} = 1100K,\ H_{feed} = 50.8mm,\ H_{sweep} = 25.4mm,\ L = 1.0mm)$

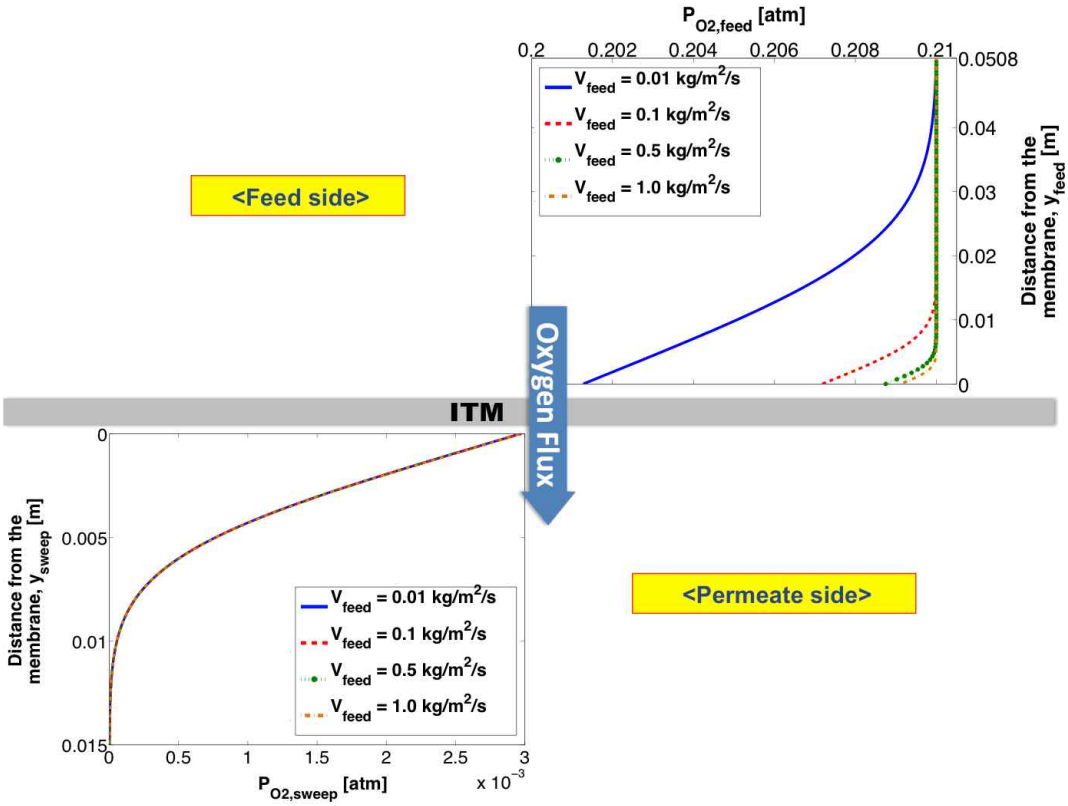

Figure 9 Spatially resolved oxygen partial pressure profiles as a function of the feed air flow rate ($V_{sweep} = 0.1kg/m^2/s$, $T_{mem} = 1100K$, $H_{feed} = 50.8mm$, $H_{sweep} = 25.4mm$, $L = 1.0mm$)

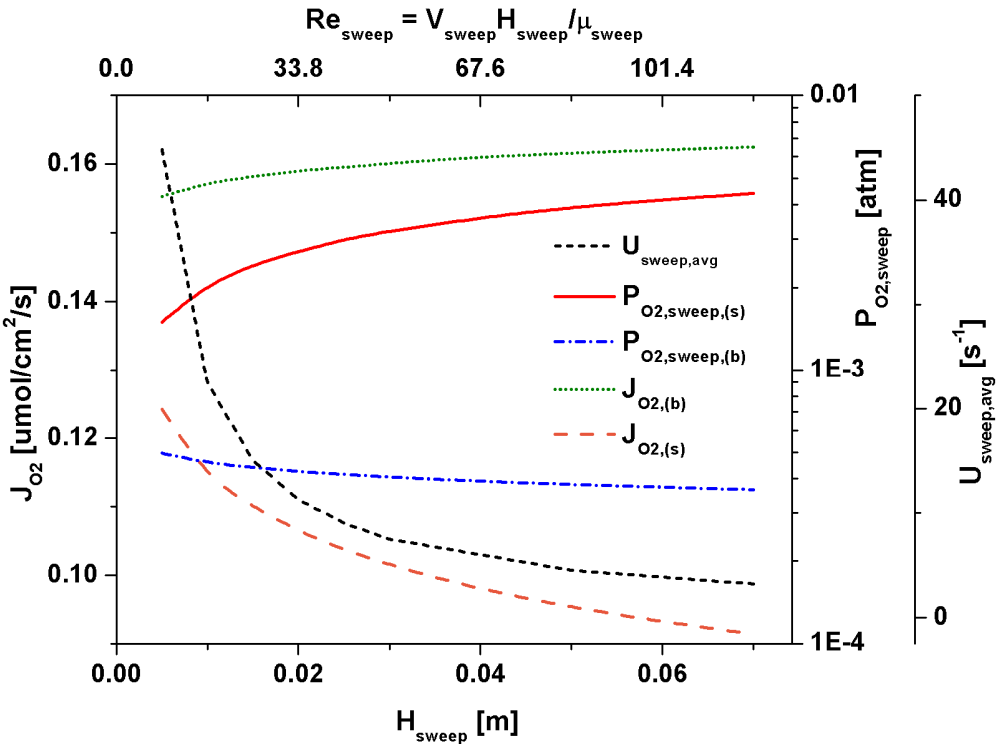

Figure 10 The effects of geometry (channel height from the membrane to the sweep gas inlet) on the oxygen permeation rate, the oxygen partial pressure on the sweep gas side and the spatially averaged parallel velocity, $U_{sweep,avg} = \frac{1}{H_{sweep}} \int_0^{H_{sweep}} U_{sweep}(t,y)dy$ ($V_{feed} = 0.1kg/m^2/s$, $V_{sweep} = 0.1kg/m^2/s$, $T_{mem} = 1100K$, $H_{feed} = 50.8mm$, $L = 1.0mm$)

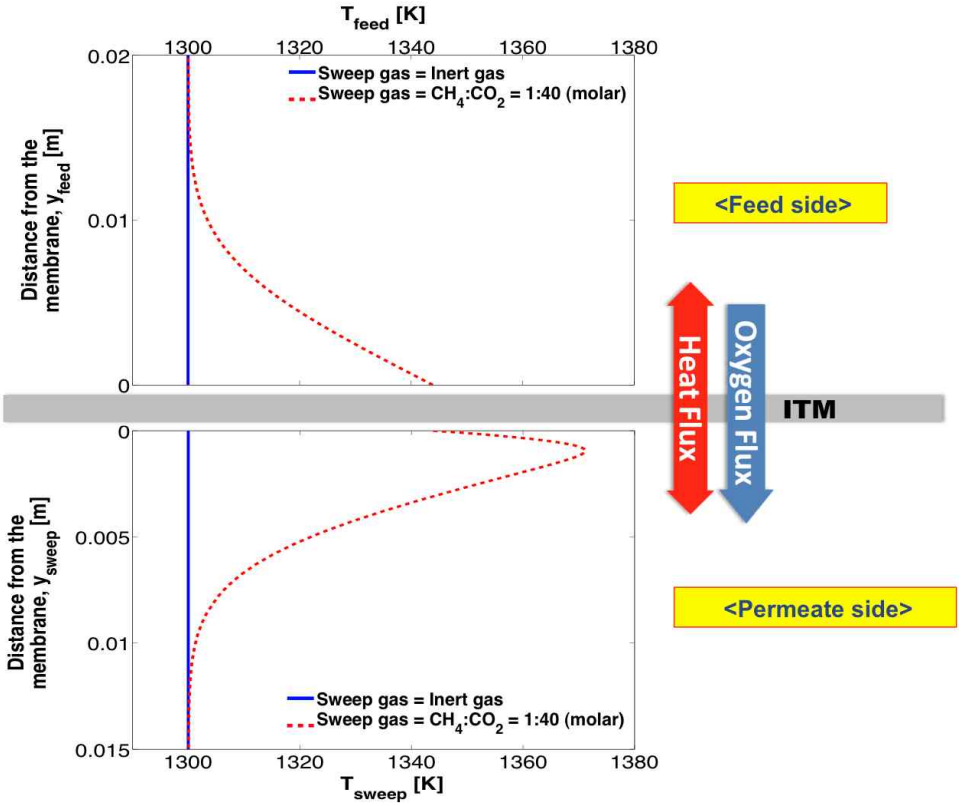

Figure 11 Temperature variations when sweep gas is inert gas or reactive gas ($V_{feed} = 0.1kg/m^2/s$, $V_{sweep} = 0.1kg/m^2/s$, $T_{in} = 1300K$, $H_{feed} = 50.8mm$, $H_{sweep} = 25.4mm$, $L = 1.0mm$)

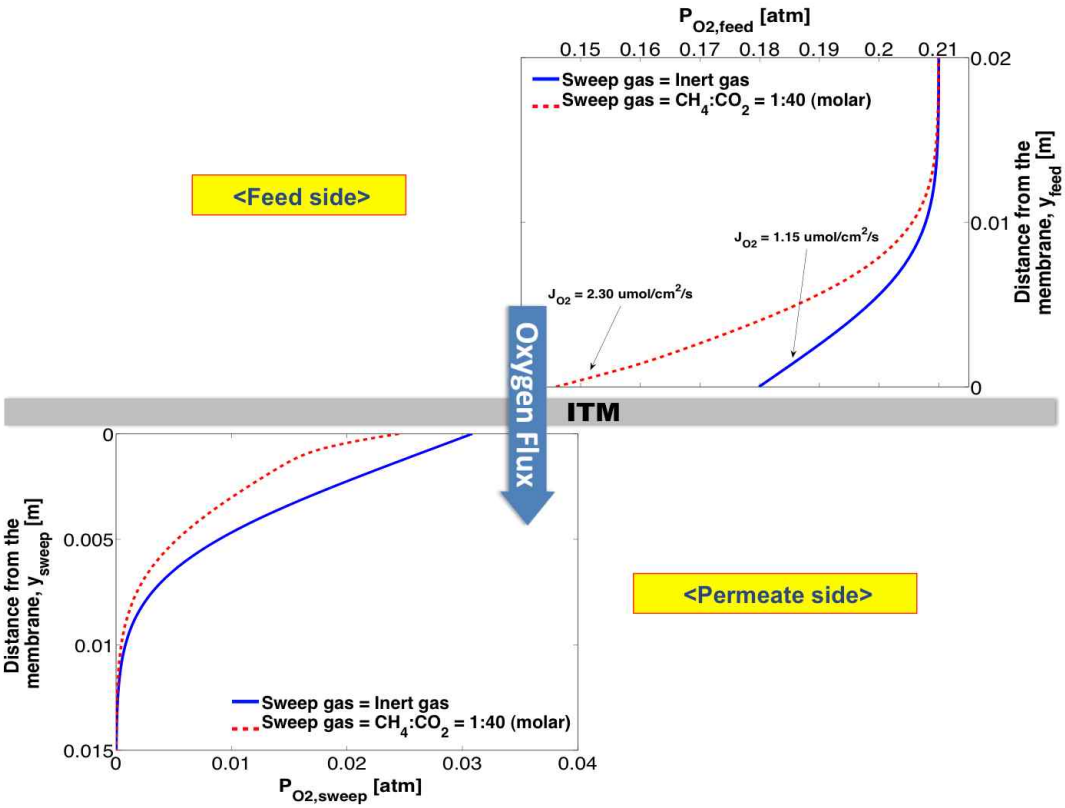

Figure 12 Spatially resolved oxygen partial pressure profiles when sweep gas is inert gas or reactive gas ($V_{feed} = 0.1kg/m^2/s$, $V_{sweep} = 0.1kg/m^2/s$, $T_{in} = 1300K$, $H_{feed} = 50.8mm$, $H_{sweep} = 25.4mm$, $L = 1.0mm$)

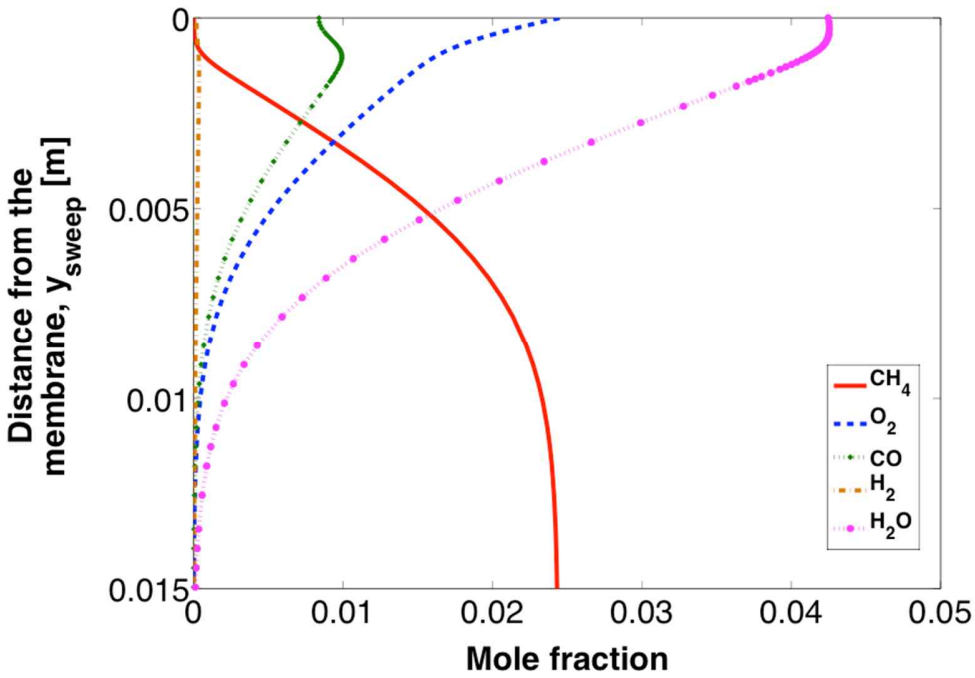

(a)

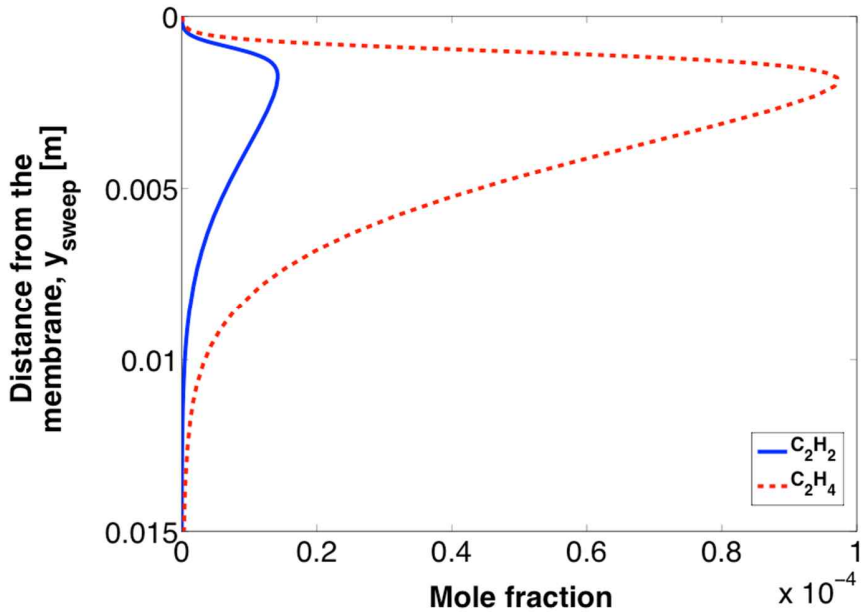

(b)

Figure 13 Influences of chemical reactions on the species concentration variations when a reactive gas is used as a sweep gas: (a) major species including CH_4, O_2, CO, H_2, and H_2O, and (b) soot precursors including C_2H_2 and C_2H_4 ($V_{feed} = 0.1kg/m^2/s$, $V_{sweep} = 0.1kg/m^2/s$, $T_{in} = 1300K$, $H_{feed} = 50.8mm$, $H_{sweep} = 25.4mm$, $L = 1.0mm$)

List of Tables

TABLE 1 EXPERIMENTAL CONDITIONS FOR OXYGEN PERMEATION RATE MEASUREMENTS BY [30]

TABLE 2 PRE-EXPONENTIAL FACTORS AND ACTIVATION ENERGIES OF $D_{V_O^{\bullet\bullet}}$, k_f AND k_r : (A) ACCOUNTING FOR THE LOCAL FLOW VARIATIONS (BASED ON $P_{O_2,feed,(s)}$ AND $P_{O_2,sweep,(s)}$) COMPUTED BY THE NUMERICAL SIMULATION AND (B) EVALUATED BY BULK STREAM PARAMETERS ($P_{O_2,feed,(b),\exp}$ AND $P_{O_2,sweep,(b),\exp}$) BY [30]

TABLE 3 FLOW PARAMETERS USED IN THE PARAMETRIC STUDY ($\mathrm{Re}_{feed} = \frac{V_{feed} H_{feed}}{\mu_{feed}}$ AND $\mathrm{Re}_{sweep} = \frac{V_{sweep} H_{sweep}}{\mu_{sweep}}$)

Table 1 Experimental conditions for oxygen permeation rate measurements by [31]

Parameter		Unit	Value
Membrane thickness	L	[cm]	0.399
Oxygen partial pressure at the feed air inlet	$P_{O_2,feed,(b),\exp}$	[atm]	$0.21 \sqcup 1.0$
Oxygen partial pressure at the sweep gas outlet	$P_{O_2,sweep,(b),\exp}$	[atm]	$4.6\times10^{-4} \sqcup 2.3\times10^{-3}$
Membrane temperature	T_{mem}	[K]	$1023 \sqcup 1223$

Table 2 Pre-exponential factors and activation energies of $D_{V_O^{\bullet\bullet}}$, k_f and k_r: (a) accounting for the local flow variations (based on $P_{O_2,feed,(s)}$ and $P_{O_2,sweep,(s)}$) computed by the numerical simulation and (b) evaluated by bulk stream parameters ($P_{O_2,feed,(b),\exp}$ and $P_{O_2,sweep,(b),\exp}$) by [31]

Parameter	Pre-exponential factor, ψ			Activation energy, E_A [J/mol]	
	Unit	Value			
		(a)	(b)	(a)	(b)
$D_{V_O^{\bullet\bullet}}$	[cm²/s]	$(1.01 \pm 0.05) \times 10^{-2}$	1.58×10^{-2}	$(7.56 \pm 0.05) \times 10^{4}$	7.36×10^{4}
k_f	[cm/atm$^{0.5}$/s]	$(9.21 \pm 0.44) \times 10^{8}$	5.90×10^{6}	$(2.68 \pm 0.005) \times 10^{5}$	2.27×10^{5}
k_r	[mol/cm²/s]	$(1.75 \pm 0.087) \times 10^{11}$	2.07×10^{4}	$(3.77 \pm 0.004) \times 10^{5}$	2.41×10^{5}

Table 3 Flow parameters used in the parametric study ($\mathrm{Re}_{feed} = \frac{V_{feed} H_{feed}}{\mu_{feed}}$ and $\mathrm{Re}_{sweep} = \frac{V_{sweep} H_{sweep}}{\mu_{sweep}}$)

Parameter		Unit	Base-case value	Range of variations	
				Min	Max
Membrane temperature	T_{mem}	[K]	1100	950	1300
Sweep gas flow rate	V_{sweep}	[kg/m^2/s]	0.1 (Re_{sweep} = 42.92)	0.005 (Re_{sweep} = 2.146)	3.0 (Re_{sweep} = 1287.6)
Feed gas flow rate	V_{feed}	[kg/m^2/s]	0.1 (Re_{feed} = 111.38)	0.001 (Re_{feed} = 1.114)	1.0 (Re_{feed} = 1113.8)
Channel height from membrane to sweep gas inlet	H_{sweep}	[mm]	25.4 (Re_{sweep} = 42.92)	5.0 (Re_{sweep} = 8.449)	70 (Re_{sweep} = 118.29)
Oxygen concentration in feed air	$Y_{O_2,feed}$	[atm]	0.21	0.21	1.0
Membrane thickness	L	[mm]	1.0	--	--
Channel height from membrane to feed gas inlet	H_{feed}	[mm]	50.8	--	--